Title

Understanding Responses of Summer Continental Daily Temperature Variance to Perturbations in the Land Surface Evaporative Resistance

Journal

Journal of Climate, 36(6)

ISSN

0894-8755

Authors

Kong, Wenwen
McKinnon, Karen A
Simpson, Isla R
et al.

Publication Date

2023-03-15

DOI

10.1175/jcli-d-21-1011.1

Understanding Responses of Summer Continental Daily Temperature Variance to Perturbations in the Land Surface Evaporative Resistance

WENWEN KONG,[a] KAREN A. MCKINNON,[a,b] ISLA R. SIMPSON,[c] AND MARYSA M. LAGUË[d]

[a] *Institute of the Environment and Sustainability, University of California, Los Angeles, Los Angeles, California*
[b] *Departments of Statistics and Atmospheric and Oceanic Sciences, University of California, Los Angeles, Los Angeles, California*
[c] *Climate and Global Dynamics Laboratory, National Center for Atmospheric Research, Boulder, Colorado*
[d] *Coldwater Lab, University of Saskatchewan Center for Hydrology, Canmore, Alberta, Canada*

(Manuscript received 30 December 2021, in final form 7 September 2022)

ABSTRACT: Understanding the roles of land surface conditions and atmospheric circulation on continental daily temperature variance is key to improving predictions of temperature extremes. Evaporative resistance (r_s, hereafter), a function of the land cover type, reflects the ease with which water can be evaporated or transpired and is a strong control on land–atmosphere interactions. This study explores the effects of r_s perturbations on summer daily temperature variance using the Simple Land Interface Model (SLIM) by mimicking, for r_s only, a global land cover conversion from forest to crop/grassland. Decreasing r_s causes a global cooling. The cooling is larger in wetter areas and weaker in drier areas, and primarily results from perturbations in shortwave radiation (SW) and latent heat flux (LH). Decreasing r_s enhances cloud cover due to greater land surface evaporation and thus reduces incoming SW over most land areas. When r_s decreases, wetter areas experience strong evaporative cooling, while drier areas become more moisture-limited and thus experience less cooling. Thermal advection further shapes the temperature response by damping the combined impacts of SW and LH. Temperature variance increases in drier areas and decreases in wetter areas as r_s decreases. The temperature variance changes can be largely explained from changes in the combined variance of SW and LH, including an important contribution of changes in the covariance of SW and LH. In contrast, the effects of changes in thermal advection variance mainly affect the Northern Hemisphere midlatitudes.

SIGNIFICANCE STATEMENT: This study aims to better understand processes governing daily near-surface air temperature variance over land. We use an idealized modeling framework to explore the effects of land surface evaporative resistance (a parameter that controls how hard it is to evaporate water from the surface) on summer daily temperature variance. We find that a uniform decrease of evaporative resistance across the global land surface causes changes in the temperature variance that can be predicted from changes in the combined variance of shortwave radiation and latent heat flux. The variance of horizontal advection is important in altering the temperature variance in the Northern Hemisphere midlatitudes. Our findings shed light on predicting the characteristics of temperature variability as a function of surface conditions.

KEYWORDS: Atmosphere-land interaction; Climate variability; Evapotranspiration; Soil moisture; Surface temperature; Land surface model

1. Introduction

Near-surface air temperature (hereafter temperature) over land has a direct impact on our everyday lives. Temperature extremes (such as heatwaves and cold spells) affect human mortality (Singh et al. 2019), agricultural yields (Vogel et al. 2019), and wildfires (Hulley et al. 2020; Ruffault et al. 2020). Greenhouse gas forcing increases mean temperatures and may also affect temperature variability (Katz and Brown 1992) in both warm (Baldwin et al. 2019; Chan et al. 2020; Kotz et al. 2021; Schär et al. 2004) and cold (Schneider et al. 2015; Screen 2014) seasons. Changes in temperature variability in a warming climate can further modify the odds and intensity of extreme temperature events (Fischer and Knutti 2015; Seneviratne et al. 2012). For example, an increase in temperature variance leads to an increased probability of hot extremes, in addition to the mean warming. However, determining likely changes in the moments of temperature at daily to synoptic time scales has been challenging, as temperature variability can be affected by perturbations in both land surface properties (Seneviratne et al. 2010) and atmospheric circulation (Branstator and Teng 2017; Wallace et al. 1995). This is particularly true of summer heat extremes (Cowan et al. 2017; Quesada et al. 2012; Rasmijn et al. 2018). Therefore, an accurate understanding of the separate contribution of the "land surface driven" and the "atmospheric driven" portion of temperature variability, and the interaction between the two drivers, is key to improve our understanding of how the occurrence and intensity of temperature extremes will evolve in the future (Schär et al. 2004). The main physical factors that govern temperature variability over land at daily time scales include fluctuations in incident radiation, land surface conditions, horizontal thermal advection, and adiabatic compression and expansion due to vertical motion of air parcels. In this study, we explore the physical drivers that control changes in the summertime continental temperature variance in response to land surface perturbations.

Supplemental information related to this paper is available at the Journals Online website: https://doi.org/10.1175/JCLI-D-21-1011.s1

Corresponding author: Wenwen Kong, wenwen.kong@berkeley.edu

DOI: 10.1175/JCLI-D-21-1011.1

Incoming radiation is a major driver of summer temperature variability (Lorenz et al. 2012; Schwingshackl et al. 2018). Schwingshackl et al. (2018) found that the incident shortwave radiation and downwelling longwave radiation could explain about 70% of summertime monthly temperature variance on interannual time scales. By constructing a diagnostic model, Vargas Zeppetello et al. (2020) identified the variance of shortwave radiation as a crucial factor in determining the summer temperature variance at monthly time scales. Incoming shortwave radiation anomalies during summer are governed by aerosol effects (Lohmann and Feichter 2005) and cloud cover (Lenderink et al. 2007; Pfahl and Wernli 2012; Vargas Zeppetello et al. 2019a). Cloudiness is often associated with anomalous atmospheric circulation patterns (Andrade et al. 2012). For example, persistent anticyclones can induce clear-sky conditions, increase incoming shortwave radiation, and trigger hot summer extremes (Meehl and Tebaldi 2004; Pfahl and Wernli 2012). Variations in downwelling longwave radiation are associated with cloud cover (Stephens and Webster 1981) and water vapor (Compo and Sardeshmukh 2009); however, the causal direction between the downwelling longwave and near-surface temperature can be complicated by the strong coupling between the two (Vargas Zeppetello et al. 2019b).

Due to the strong land–atmosphere coupling[1] during summer, land surface conditions can alter near-surface climate through energy and water fluxes (Dirmeyer 2003). In particular, soil moisture can affect temperature variance by modifying the partitioning of the surface turbulent energy fluxes (Delworth and Manabe 1989). Soil thermal inertia also plays a major role on the day-to-day variability of near-surface air temperature in water-limited regions (Cheruy et al. 2017). Based on the dependence of evapotranspiration on soil moisture amount, land–atmosphere coupling can be categorized into three evaporative regimes (Seneviratne et al. 2010). A dry regime is where the soil moisture amount is below the wilting point under which it is difficult for the plants to extract water from the soil. A water-limited regime is where the evapotranspiration is strongly constrained by the soil moisture availability: more soil moisture leads to larger evaporative fraction. An energy-limited regime is where evapotranspiration is largely controlled by atmospheric processes, such as incoming radiation, boundary layer wind speed, and temperature, instead of soil moisture availability. Among the three evaporative regimes, it is the water-limited regime in which soil moisture exerts a strong control on temperature variability by affecting the partitioning between latent and sensible heat fluxes (Seneviratne et al. 2010). Both observational analysis (Hirschi et al. 2011) and model simulations (Jaeger and Seneviratne 2011) have demonstrated impacts of soil moisture amount on temperature extremes. Comparison of regional climate simulations between coupled and prescribed soil moisture reveals an amplified spatial and temporal extent of several European heat wave events when land–atmosphere coupling is active (Fischer et al. 2007a). Spring precipitation and soil moisture deficits were suggested to contribute to the development of the 2003 European summer heatwave (Fischer et al. 2007b). The depletion of soil moisture within the summer season and the increased sensitivity of evaporation to soil moisture perturbations is suggested to contribute to the model predicted increase in summer temperature variability over the Northern Hemisphere midlatitudes under climate change (Chan et al. 2020; Fischer and Schär 2009; Seneviratne et al. 2006). Besides the variance, many studies have discussed impacts of land–atmosphere interaction on the mean climate as well. For example, land-use and land-cover change could affect near-surface air temperatures (Luyssaert et al. 2014; de Noblet-Ducoudré et al. 2012; Pitman et al. 2009), and land management has been proposed as a mitigation strategy for future warming (Canadell and Raupach 2008). Findell et al. (2007) found that simulated changes in surface albedo, roughness, and evaporative resistance resulting from a conversion from forest to grassland could cause surface warming in perturbed regions through changes in the surface radiative and turbulent fluxes and through atmospheric feedbacks. Changes in land surface conditions can also impact remote regions through cloud feedbacks and atmospheric teleconnections (Devaraju et al. 2018; Kooperman et al. 2018; Laguë and Swann 2016; Swann et al. 2012).

Unlike the winter season when the horizontal temperature advection (guided by the location of the westerlies and storm tracks) accounts for the occurrence of warm and cold temperature extremes (Garfinkel and Harnik 2017), temperature advection is not generally thought to be a dominant control on summer temperature variance due to the weaker equator-to-pole temperature gradient. Holmes et al. (2016) found that the role of thermal advection in future changes in summer temperature variability is small and mostly confined to Europe and coastal areas. However, Linz et al. argued that temperature advection can play an essential role in summer temperature variability, although they concluded this based on highly idealized modeling frameworks. Linz et al. (2018) invoked a link between thermal advection and summer temperature variance in the Southern Hemisphere through an advection–diffusion model, while Linz et al. (2020) argued that thermal advection dominates the midlatitude temperature variance response to increasing carbon dioxide in an aquaplanet world. Further, Tamarin-Brodsky et al. (2020) suggested a purely dynamical mechanism exists that shapes the changes in temperature variability, evidenced by the coherent changes in the moments in the lower atmospheric temperature (850 hPa) and near-surface air temperature in climate models.

Despite the above-mentioned advances, a quantitative understanding of contributions of land conditions, atmospheric processes, and the feedback between the two in modulating daily summertime temperature variability is lacking. Even less clear is if and how the underlying physical processes governing the temperature distribution would change in a changing climate. Though we cannot fully address these gaps in the current paper, our work is motivated and guided by these overarching questions. In this study, we focus on understanding

[1] Here, "coupling" refers to the degree one variable controls another, and "land–atmosphere coupling" refers to the land surface condition control on the near-surface atmosphere through surface energy and water fluxes.

the basic effects of one land surface property, the land surface evaporative resistance (r_s, hereafter), on the first two moments (mean and variance) of summer temperature over land. We focus on the r_s control on summer temperature distributions because it effectively alters the land–atmosphere coupling and soil moisture amount by controlling evaporative efficiency. Further, although the r_s perturbations that we investigate in this study are considerably larger and more idealized than predicted changes under climate change and more global than anything that happens in reality, understanding of the physical pathways that mediate the r_s control on summer temperature distributions increases our basic understanding of how changes in land surface properties affect near-surface temperature. Our approach of focusing on the effects of a single land surface property is analogous to other simplified modeling frameworks that are used to better understand the climate response to perturbations (Jeevanjee et al. 2017). We utilize the Simple Land Interface Model (SLIM; Laguë et al. 2019) to explore how decreases in r_s modify the temperature variance over land and identify the underlying physical processes involved. Unlike complex land surface models such as the Community Land Model version (CLM; Lawrence et al. 2019) where most land surface properties are emergent and result from the simulated representation of complex biogeophysical processes, SLIM offers a greater degree of control allowing us to separate the effects of individual land surface properties. In particular, we want to turn a single, important knob (e.g., r_s) and examine its effects on the partitioning of surface turbulent heat fluxes to understand its impacts on temperature variability. We cannot achieve this in a complex land surface model like CLM because vegetation cover changes in CLM result in simultaneous changes in more than one land surface property; thus, the resulting temperature response will be a function of changes in many different processes. Our work aims for a process-level understanding made possible by a simplified model like SLIM, which allows us to perturb each land surface property separately. Laguë et al. (2019) have demonstrated the utility of SLIM to aid in understanding of the impacts of land surface properties on the climatological terrestrial surface energy budget and global climate. Our work is distinct from previous studies on the climatic effects of r_s perturbations in SLIM (Kim et al. 2020; Laguë et al. 2019, 2021) because the focus of these earlier studies is on the response of mean climate (as opposed to the temperature variance) to the r_s perturbations.

We note that our modeling framework also differs from the Global Land–Atmosphere Coupling Experiment (GLACE) project (Guo et al. 2006; Koster et al. 2006). The GLACE-CMIP5 protocol (Seneviratne et al. 2013) was designed to assess the effects of changes in the variability of soil moisture without changing the seasonal cycle of soil moisture climatology. The impacts of soil moisture–atmosphere coupling on temperature variability in GLACE is determined by comparing the simulated temperature variability between a prescribed soil moisture simulation and an interactive soil moisture simulation. The two-way coupling between soil moisture and the atmosphere is disabled in the prescribed soil moisture experiment by overriding soil moisture with the climatological seasonal cycle at each time step. In contrast, we allow for realistic interactions between the land surface and the atmosphere, thereby r_s perturbations in our simulations change the soil moisture, evaporation, and precipitation in a physically consistent manner that conserves the balance of liquid water. This avoids some of the challenges in the GLACE experimental design such as a lack of water conservation and an associated unrealistic precipitation response in some regions (Berg et al. 2014).

The remainder of this paper is organized as follows. After describing the data, methods, and model experiments in section 2, we will first discuss changes in the summer mean state and changes in the land–atmosphere coupling as evaporative resistance decreases in section 3. We then focus on the responses of summer daily temperature variance to decreases in r_s in section 4. We will demonstrate that changes in the temperature variance in the context of our simulations can be largely understood through a surface energy balance perspective, while contributions from changes in the thermal advection are concentrated over the extratropical land areas. We discuss the similarity and differences between our diagnostic framework and previous studies in section 5 before providing a summary in section 6.

2. Data, model, and experiments

a. Data

We use the 1979–2019 daily latent heat flux, sensible heat flux, and 2-m air temperature from the fifth generation of the ECMWF atmospheric reanalysis dataset (ERA5) (Hersbach et al. 2020) to validate the fidelity of SLIM simulated climate and temperature variability (see the appendix). We used the bilinear interpolation to interpolate the ERA5 variables from 0.25° × 0.25° resolution to the 0.9° × 1.25° grid of the Community Earth System Model 2 (CESM2) resolution prior to analysis. While the surface fluxes from ERA5 are primarily model generated, it is found that the overestimation of the surface latent heat flux has been improved in ERA5 compared to its predecessor ERA-Interim (Martens et al. 2020). The monthly actual evaporation and potential evaporation from the Global Land Evaporation Amsterdam Model (GLEAM) v3.5a dataset (spanning 1980–2020) (Martens et al. 2017; Miralles et al. 2011) are also used as an alternative observation-based estimate of the spatial distribution of evaporative fraction.

b. Model and experiments

SLIM bears strong resemblance to early land surface models (Bonan 1996; Manabe 1969; Milly and Shmakin 2002). It is coupled to CESM2 (Danabasoglu et al. 2020) and can be run within the CESM framework in place of the Community Land Model version 5 (CLM5) (Lawrence et al. 2019). A complete documentation of SLIM has been provided by Laguë et al. (2019). In a nutshell, SLIM solves a linearized bulk surface energy budget. It uses a bucket model for hydrology and a simple snow model for wintertime land-albedo feedbacks. SLIM reads in user-defined land surface properties (such as soil properties and vegetation cover related surface parameters, etc.; see more in the following paragraph and the online supplemental material) as prescribed boundary conditions. We use 10 ensemble members of CESM2 (Danabasoglu et al. 2020) that were contributed to phase 6 of the Coupled Model

Intercomparison Project (CMIP6) Atmospheric Model Intercomparison Project (AMIP) (Community Earth System Model developers and affiliates 2019) to derive surface property inputs for SLIM.[2] The CESM2 AMIP simulations span from 1950 to 2014 and are run with prescribed sea surface temperatures (SSTs) and sea ice, and forced with observed historical forcing (Danabasoglu et al. 2020). The land component of the AMIP runs is CLM5 (Lawrence et al. 2019) and the atmospheric component is the Community Atmospheric Model version 6 (CAM6; Bogenschutz et al. 2018). We used the 1991 to 2010 climatology (averaged across the 10 ensemble members) to generate SLIM inputs.

To provide relatively realistic land surface conditions, we allow spatial variation of several surface properties that vary with soil type and vegetation, such as soil thermal conductivity and heat capacity, snow masking depth, and soil water bucket depth. This approach differs from Laguë et al. (2019) where all land surface properties are prescribed uniformly. Note that the prescribed soil water bucket depth denotes the maximum water each grid cell can hold (see the online supplemental material for details), and our simulated soil moisture refers to the amount of soil water in the bucket hydrology model used in SLIM. Unlike the real-world situation where the land surface conditions vary with season, we kept all the land surface properties fixed throughout the year in our simulations. However, despite the simplification, the SLIM simulated summer climatology and variability are comparable to the comprehensive land surface model (e.g., CLM5) and reanalysis datasets [see Laguë et al. (2019) and also our appendix]. Future work merits incorporating the seasonality of land surface conditions in this modeling framework. We summarize the derivation of each land surface property in the supplemental material, and code for the forcing file generation can be found in the data availability statement at the end of this article.

We run SLIM at 1.9° × 2.5° resolution with the CESM2 component set F2000climo, in which SLIM is coupled with CAM6, and SSTs and sea ice that are representative of the year 2000 are prescribed. We conduct three simulations where the global evaporative resistance is uniformly prescribed at 20, 150, 1000 s m^{-1}; these runs are called r_s20, r_s150, and r_s1000. These values roughly correspond to the evaporative resistance that is representative for wheat, corn, and Jack pine, respectively [based on Fig. 17.10 in Bonan (2016)]. Note that though albedo, surface roughness, and aerodynamic resistance also vary with the land cover type in the real world (Lee et al. 2011; Pitman 2003), the only difference in the land surface boundary condition across our simulations is the prescribed magnitude of the evaporative resistance. Each simulation is integrated for 45 years; we use the last 40 years for analysis.

c. Evaporation in SLIM

We begin by briefly introducing the controlling factors of the latent heat flux in SLIM, which are of direct relevance to our study. SLIM simulates the land surface hydrology using a bucket model, where the water holding capacity is prescribed (Laguë et al. 2019). Latent heat flux (LH) in SLIM can be affected by several factors:

$$\mathrm{LH} = \rho_{\mathrm{air}} L_v (q_s - q_{\mathrm{ref}}) \beta / r_{aw}, \tag{1}$$

where ρ_{air} is the density of air, L_v is the latent heat of vaporization, q_s is the surface humidity, and q_{ref} is the atmospheric humidity at reference height. Equation (1) suggests that besides the near-surface humidity gradient, two other factors control evaporation in the model. One is the aerodynamic resistance for moisture (r_{aw}; $r_{aw} = r_s + r_{ah}$) which combines both the aerodynamic resistance for heat (r_{ah}) and the prescribed bulk evaporative resistance (r_s), with r_s being the parameter that we perturb in our simulations. The other is a time-varying β factor that measures the fullness of the water bucket. The implementation of the β factor was motivated by empirical observations (Budyko 1961) and has been used in early land surface models (Manabe 1969; Milly and Shmakin 2002). The β factor parameterization is kept the same across our simulations. Note that β is equal to 1 when the bucket is more than 75% full; when the bucket is less than 75% full, β ranges between 0 and 1 (the emptier the bucket, the lower the β) and introduces additional resistance to capture the increased difficulty in evaporating water from increasingly dry soils. Thus, we expect competing effects on evaporation from the prescribed r_s and the water bucket emptiness β in a low r_s scenario: a decrease in r_s enhances evaporation efficiency and thus reduces soil water in the bucket; when the bucket fullness becomes less than 75%, β decreases and introduces an additional resistance to the evaporation. While acknowledging that the parameterization of LH is a simplification of the reality, the competing effects between r_s and the β factor do exist in regions where vegetation features lower evaporative resistance. For example, Teuling et al. (2010) show that compared to forests, grasslands initially transpire more water when there is high net radiation at the surface. As a result, soils in grasslands dry more quickly, which can ultimately limit further evaporation.

d. Methods

In the following, we use SLIM to refer to the land–atmosphere coupled simulations using SLIM coupled with CAM6. We focus on austral [December–February (DJF)] and boreal [June–August (JJA)] summer. We show results from JJA in the Northern Hemisphere, and DJF in the Southern Hemisphere in the same panels, and we use a gray horizontal line in our map view figures to indicate the equator. We obtain the summer daily anomalies [denoted with the prime symbol (′)] by removing the annual cycle of the daily climatology. We use the Fourier transform harmonics instead of the empirical annual cycle calculated from daily climatology to represent the seasonal cycle because it gives a smoother estimate. Since more harmonics are needed for capturing an accurate annual cycle of surface energy fluxes, we use the first 10 harmonics of the daily climatology of each variable to represent their respective annual cycles (see Fig. S4 in the online supplemental material). For ease of presentation, we focus on the comparison between r_s20 and r_s1000, while

[2] Note that all 10 ensemble members can be accessed from NCAR's Cheyenne campaign storage (see the data availability statement).

r_s150 is used to validate SLIM's performance in the appendix. When assessing changes in the mean state, we use the two-sided Student's t test to test the null hypothesis that the sample means are from the same population; the associated degrees of freedom is 38, as we treat each summer seasonal mean as independent. When evaluating the variance change, we use the F test (von Storch and Zwiers 1999) to test the null hypothesis that the sample variances are from the same population. Unless stated otherwise, hatched areas in the figures presented indicate regions where changes are not significant after accounting for multiple hypothesis testing by controlling for a false discovery rate of 0.1 (Wilks 2016).

3. Changes in the mean state and land–atmosphere coupling

Before assessing the temperature variance response to the r_s perturbation, we first discuss changes in the summer climatology of land surface hydrology (section 3a), temperature, and surface energy fluxes (section 3b), as well as the soil moisture–atmosphere coupling strength (section 3c).

a. Land surface hydrology

Figures 1a–c show the SLIM simulated summertime soil moisture climatology for r_s20, r_s1000, and their difference (i.e., $r_s20 - r_s1000$). The red contour in Figs. 1a and 1b denotes the soil moisture isoline of 100 kg m^{-2} in each simulation. We highlight the location where the summer climatology of soil moisture amount is equal to 100 kg m^{-2} to show that the spatial extent of relatively dry areas (i.e., for visualization purposes, locations with soil moisture less than 100 kg m^{-2}) has expanded in r_s20. As r_s decreases, soil moisture decreases over all land areas except for part of the Amazon (Fig. 1c). The magnitude of the soil moisture reduction is not spatially uniform, because decreasing r_s is less effective at changing soil moisture in regions where the background soil moisture is already very limited, such as the Sahara and the Arabian Peninsula. The reduction of soil moisture in the Northern Hemisphere high latitudes is also small, because of the enhanced precipitation in those areas (Figs. 1f,g), as discussed below.

We examine changes in the summer precipitation, evaporation, and spring soil moisture anomalies to further understand changes in summer soil moisture. Runoff is also important for the hydrology budget; however, the difference in the runoff between r_s20 and r_s1000 is negligible and thus not shown here. The minimal change in runoff might be related to the usage of a bucket model for hydrology in SLIM, where runoff only occurs when the amount of soil water exceeds the prescribed bucket depth (Laguë et al. 2019). Despite the globally uniform r_s perturbation, changes in the evaporation exhibit a strong geographical dependence: wetter regions experience enhanced evaporation while evaporation reduces in relatively dry regions (Fig. 1e). While decreases in r_s might be expected to increase evaporation everywhere, we see that this behavior is only observed in wet regions. In dry regions, decreases in mean state soil moisture brought on by lower r_s exert a bigger driver of evaporation than our prescribed changes in r_s (see section 2c on effects of the β factor, i.e., the additional resistance brought by the bucket's emptiness level in dry areas). Associated with the large changes in evaporation, we also see a general increase in precipitation, such that precipitation minus evaporation ($P - E$) is positive over much of the Northern Hemisphere continental area (Fig. 1g). The increase in the soil moisture in the Amazon is related to the large increase in precipitation and the resulting positive $P - E$ (Figs. 1g,h). We note that changes in soil moisture do not closely follow changes in $P - E$ during summer. This is because we reduced r_s all year round, such that soil drying is already pronounced during spring (Fig. 1d; also see Fig. S5 for the annual cycle of soil moisture). Therefore, changes in the soil moisture and $P - E$ from earlier seasons (e.g., Figs. 1d,h) also contribute to the summer soil moisture response.

b. Near-surface air temperature and surface energy flux

Decreases in r_s cool the 2-m air temperature (T_{2m}) over almost all land regions (Fig. 2a). The cooling magnitude is most substantial in wet regions where evaporation increases the most and is smaller in relatively dry regions. Changes in surface temperature (T_s) (Fig. 2b) are almost identical to changes in T_{2m} though with a slightly larger magnitude. We employ the surface energy balance to discuss why decreasing r_s cools T_{2m} and why the cooling magnitude differs between relatively dry and wet regions. Our discussion here is diagnostic and the following interpretation is based on the equilibrium state when temperature and the surface energy budget have reached a new balance.

The surface energy balance can be written as

$$\mathrm{SW}_n\downarrow + \mathrm{LW}_d\downarrow = \mathrm{LW}_u\uparrow + \mathrm{LH}\uparrow + \mathrm{SH}\uparrow + G\downarrow, \qquad (2)$$

where the arrows indicate the defined direction of each energy flux term, $\mathrm{SW}_n\downarrow$ denotes net shortwave radiation at the surface, $\mathrm{LW}_d\downarrow$ denotes downwelling longwave radiation, $\mathrm{LW}_u\uparrow$ denotes upwelling longwave radiation, LH↑ is latent heat flux, SH↑ is sensible heat flux, and $G\downarrow$ denotes ground heat flux. We drop the arrows in the following for simplicity. As the surface albedo is prescribed across our simulations,[3] SW_n and the incoming shortwave radiation behave in a consistent fashion, and only SW_n is shown. In the following, we discuss how changes in the surface energy fluxes affect the temperature response by first presenting responses in the surface radiative fluxes and then discussing responses in the surface turbulent heat fluxes.

Overall, changes in SW_n primarily occur in the Northern Hemisphere (Fig. 2c). Decreasing r_s results in an evident decrease of SW_n in the northern high latitudes and several low-latitude land areas such as Southeast Asia and the Amazon. The western United States, central Asia, and central Africa receive more shortwave radiation in the low r_s case. Changes in SW_n are primarily due to changes in cloud cover[4] because

[3] There are a few exceptions in the Arctic area where the summertime snow cover difference between r_s20 and r_s1000 has led to slight changes of surface albedo across the simulations.

[4] Changes in the column water vapor could also affect the atmospheric transfer of shortwave radiation, but its effects are small compared to changes in cloudiness.

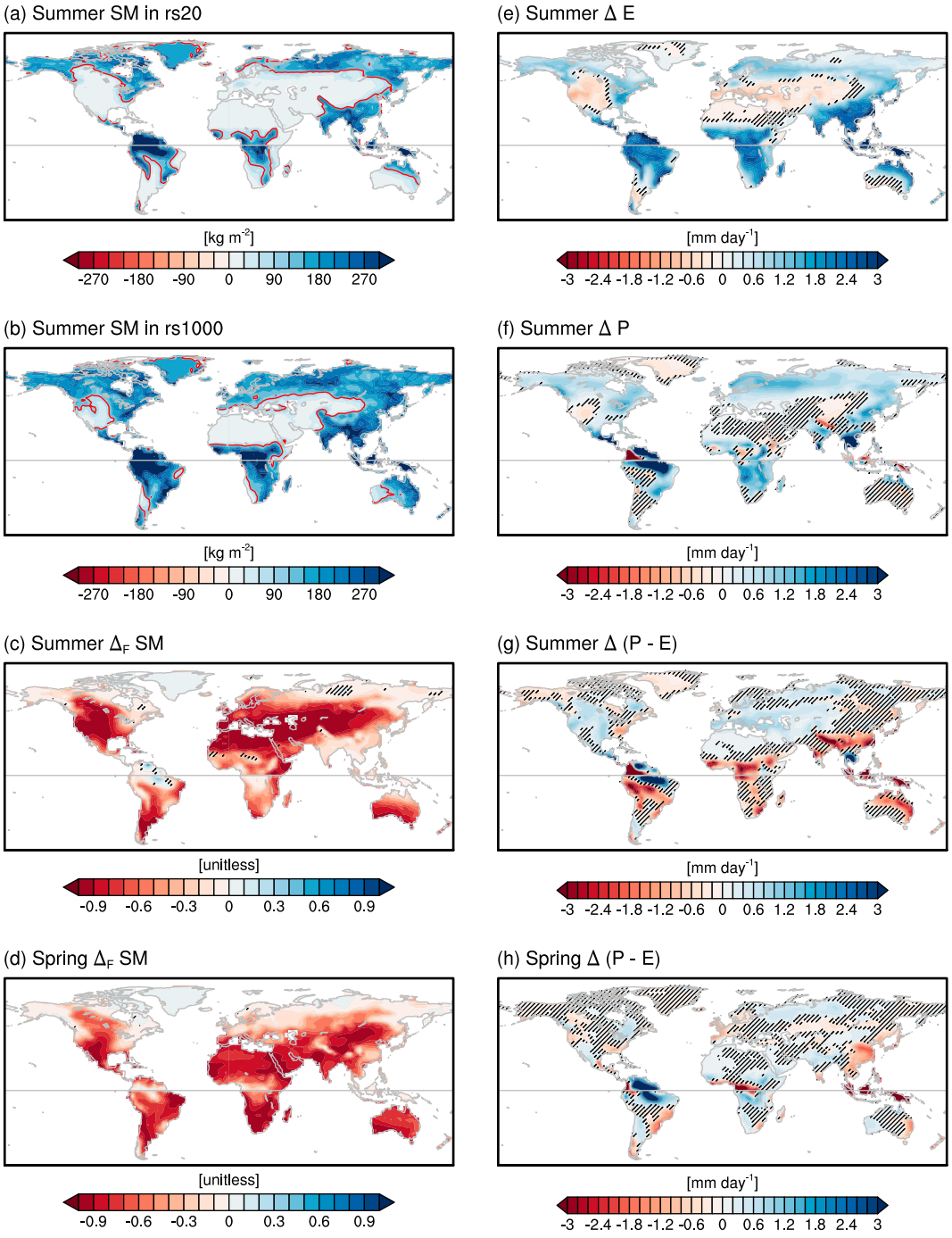

FIG. 1. The climatology of land surface hydrology. Summer climatology of soil water (kg m^{-2}) in (a) r_s20 and (b) r_s1000, and the fractional changes [$\Delta_F = (r_s20 - r_s1000)/r_s1000$] in the soil water climatology in (c) summer and (d) spring. Also shown are changes ($\Delta = r_s20 - r_s1000$) of (e) summer evaporation, (f) summer precipitation, (g) summer $P - E$, and (h) spring $P - E$. Red contours in (a) and (b) denote the soil moisture isoline of 100 kg m^{-2} in each simulation.

surface albedo is fixed across our simulations. We present changes in the cloud fraction at different altitude levels in Figs. 3a and 3c. Decreases in r_s increase low cloud fraction, particularly at northern high latitudes, which is consistent with previous findings (Kim et al. 2020; Laguë et al. 2019). Middle cloud and high cloud also increase in the Northern Hemisphere high latitudes but decrease in drier land areas. We calculate the surface cloud radiative forcing (CF) by subtracting the clear-sky from the full-sky net surface radiative fluxes, and the net CF (Fig. 3f) is the sum of the shortwave

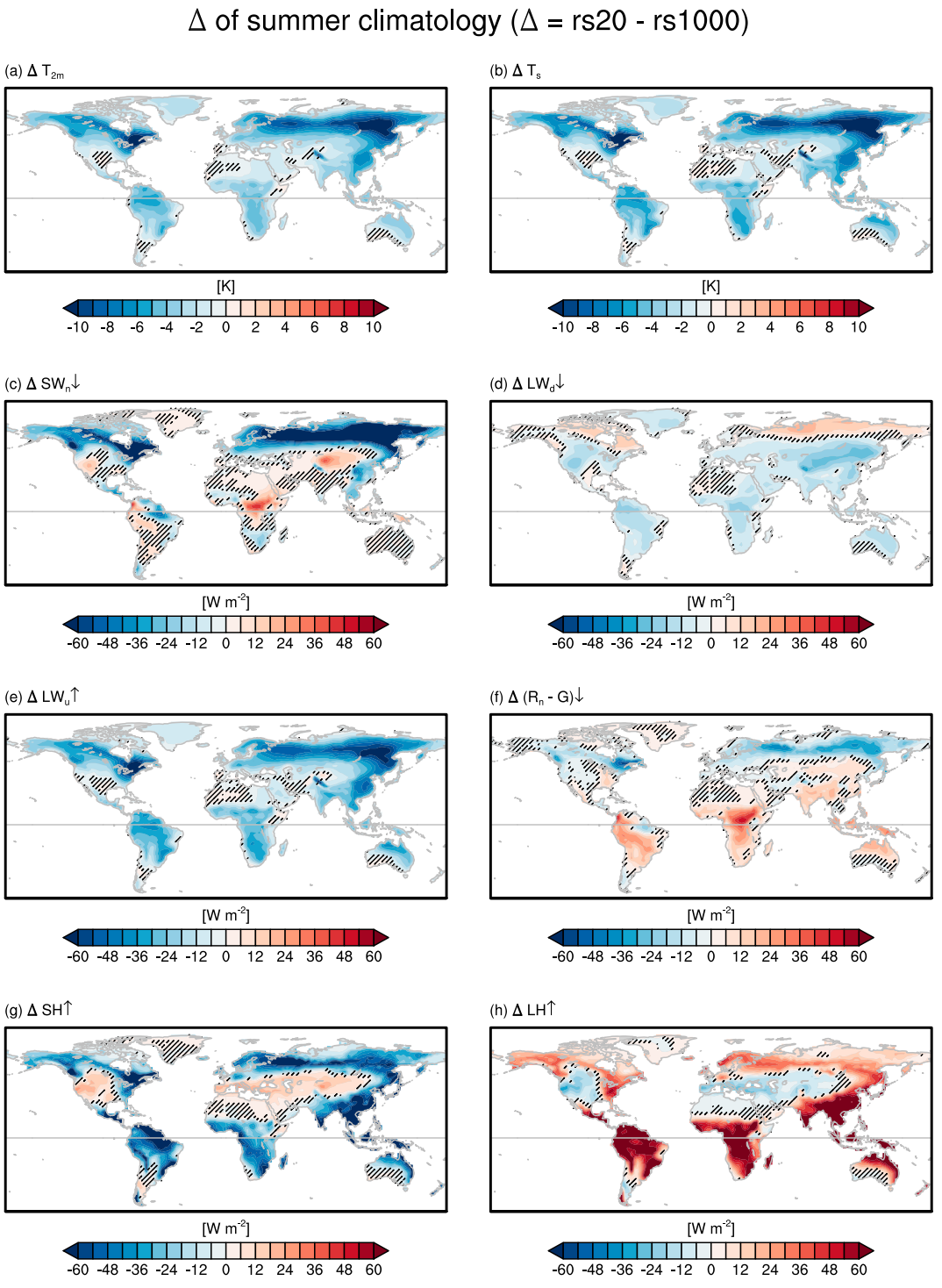

FIG. 2. The $r_s20 - r_s1000$ difference in summer climatology of temperature and surface energy fluxes. (a) T_{2m}, (b) T_s, (c) net shortwave radiation (SW_n; positive downward), (d) downwelling longwave radiation (LW_d; positive downward), (e) upwelling longwave radiation (LW_u; positive upward), (f) net radiation minus ground heat flux ($R_n - G$; positive downward), (g) sensible heat flux (SH), and (h) latent heat flux (LH). Units: K for temperature, and W m^{-2} for energy fluxes.

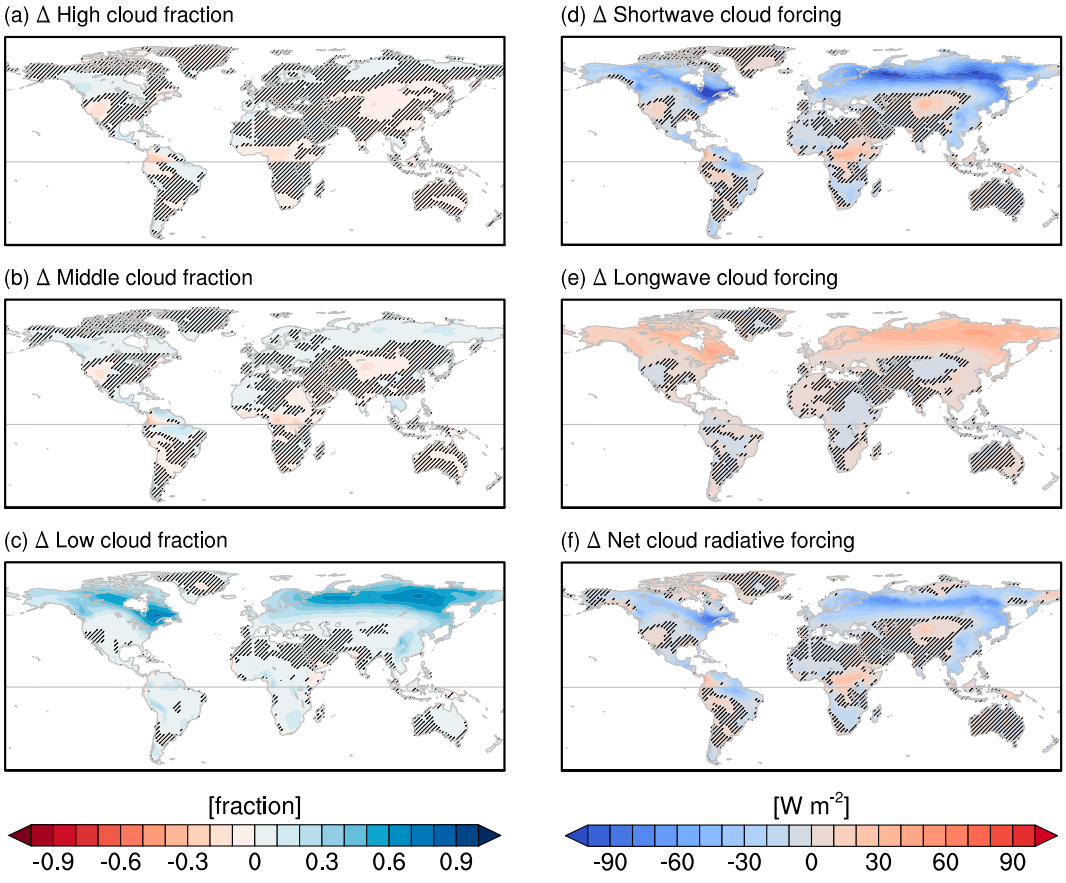

FIG. 3. (a)–(c) The $r_s20 - r_s1000$ difference in summer cloud fraction (unitless) and (d)–(f) cloud radiative forcing (W m^{-2}).

cloud radiative forcing (CF_{SW}) (Fig. 3d) and the longwave cloud radiative forcing (CF_{LW}) (Fig. 3e). Note that Figs. 3d–f reflect changes in surface radiative forcing caused by changes in cloud fraction at all levels. Negative CF suggest a surface cooling effects due to cloud change (less energy into the surface), and positive CF suggests a surface warming effects (more energy into the surface). In agreement with changes in SW_n, Fig. 3d further suggests that the global decrease in r_s can affect surface temperature through alterations in the shortwave cloud radiative forcing. These results agree with previous findings that changes in the vegetation cover, which would alter evaporation, can also alter the cloud cover and thus perturb surface shortwave forcing (Laguë and Swann 2016). Changes in the downwelling longwave (LW_d) and upwelling longwave (LW_u) are shown in Figs. 2d and 2e. Changes in LW_u reflect changes in surface temperature given that the longwave emissions from the surface are directly related to the surface temperature (Figs. 2a,b). LW_d and near-surface air temperature are also strongly coupled together such that LW_d can reflect changes in the temperature of the lower atmosphere (Vargas Zeppetello et al. 2019b). Figure 2d shows that increases in LW_d only occur in the northern high latitudes and part of the southern United States and western Africa. The decrease of LW_d over the other land areas is likely due to the cooling of near-surface air. The net longwave cloud radiative forcing (Fig. 3e) is closely related to changes in the cloud cover at higher altitudes: a warming effect results from the cooler outgoing longwave emission caused by increased middle to high cloud cover, and vice versa (Figs. 3a,b). Figure 3e shows evident positive longwave cloud radiative forcing over the northern high latitudes, suggesting that it is the increase in the middle and high cloud fraction (Figs. 3a,b) that dominate the long wave warming effect over those areas. On the other hand, increases of low cloud fraction might have contributed to the longwave radiative cooling over southwestern North America, central Africa, and central Asia (Figs. 3c,e). The net radiative effect of changes in cloud cover is to cool most land areas and to warm central Asia, the western United States, and central Africa (Fig. 3f). Figure 2f presents $\Delta(R_n - G)$; the spatial pattern of $\Delta(R_n - G)$ is nearly identical to that of ΔR_n as the change in the ground heat flux is small (not shown). The disparity between changes in the sign of ΔT_{2m} (Fig. 2a) and $\Delta(R_n - G)$ (Fig. 2f) in wet regions primarily arises from changes in the partitioning of surface turbulent heat fluxes. For example, there is a cooling response over the Northern Hemisphere subtropical land areas and the Southern Hemisphere despite the positive net radiation anomalies (Figs. 2a,f). This is consistent with an increase in the partitioning toward latent heat fluxes (Fig. 2h) in these

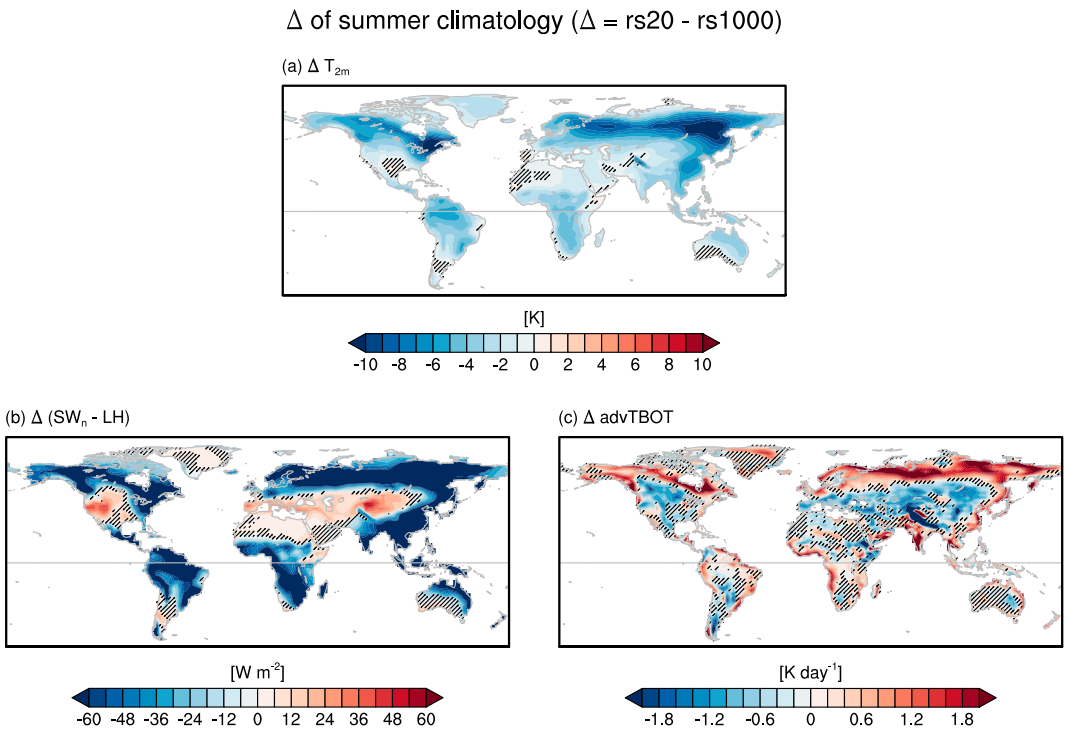

FIG. 4. (a) ΔT_{2m} [the same as Fig. 2a; we keep it here for visual comparison with (b) and (c)], (b) $\Delta(SW_n - LH)$, and (c) ΔadvTBOT (changes in the horizontal thermal advection at the model's bottom level).

regions. In contrast, the cooling in dry lands is likely due to advection, discussed further below in section 3c.

Taken together, we argue that the combined effects of the shortwave radiation and latent heat flux appear to dominate the spatial distribution of the cooling magnitude (Figs. 4a,b). Compared to other surface energy fluxes, shortwave radiation and latent heat flux are more closely affected by r_s perturbations. In particular, changes in r_s can directly alter latent heat flux (through changes in evaporation) and indirectly alter shortwave radiation (through changes in the cloudiness caused in part by changing moisture availability). We thus view changes in $(SW_n - LH)$ as surface energy forcing that controls the temperature response. In contrast, we view changes in other surface energy fluxes as the response to changes in LH and SW_n since they depend on temperature itself. However, comparison of Figs. 4a and 4b makes it clear that $\Delta(SW_n - LH)$ is not the only factor that determines ΔT_{2m}: while the spatial patterns are similar (the centered pattern correlation between the two maps is 0.74), the mean value is not, with ΔT_{2m} showing a global cooling while $\Delta(SW_n - LH)$ tends to be positive in drier regions. To understand why, we next explore effects of changes in horizontal temperature advection on ΔT_{2m}.

c. Role of horizontal thermal advection

Changes in r_s could indirectly affect T_{2m} and its variability by altering temperature advection, and we investigate this possibility here. We calculate daily horizontal temperature advection using $-\mathbf{u} \cdot \nabla T$, where $\mathbf{u}$ denotes daily horizontal winds, T denotes daily air temperature at the vertical level of interest, and ∇ denotes the horizontal gradient operator. Throughout this study, we only present horizontal thermal advection along the lowest hybrid-sigma level of the atmospheric model (around 50-m height) (denoted as advTBOT, where TBOT denotes air temperature at that level). Thermal advection at 850 hPa yields similar results (not shown). The opposite sign of $\Delta(SW_n - LH)$ (Fig. 4b) and ΔadvTBOT (Fig. 4c) over the majority of land regions suggest that changes in the horizontal thermal advection can dampen the effects of $\Delta(SW_n - LH)$. In particular, cold temperature advection anomalies coincide with the enhanced $\Delta(SW_n - LH)$, thus dampening the surface warming and eventually lead to small cooling signals. These changes in the horizontal temperature advection primarily arise from changes in the horizontal temperature gradients, which are due to the nonuniform $(SW_n - LH)$ and temperature response to decreases in r_s (Figs. 4a,b). Changes in the meridional temperature gradient are particularly pronounced and mainly occur in the northern mid- to high latitudes (Fig. S6a; see also Fig. 4a). In contrast, changes in the zonal temperature gradient are relatively small and are mostly confined to coastal and elevated regions, as well as areas that experienced nonuniform cooling responses along the zonal direction such as Siberia (Fig. S6b). Note that one can attempt to convert temperature advection into energy flux units (W m^{-2}) by making some assumptions. This is very likely not quantitatively accurate and dependent on the assumptions being made, but it can at least give an indication that the magnitude

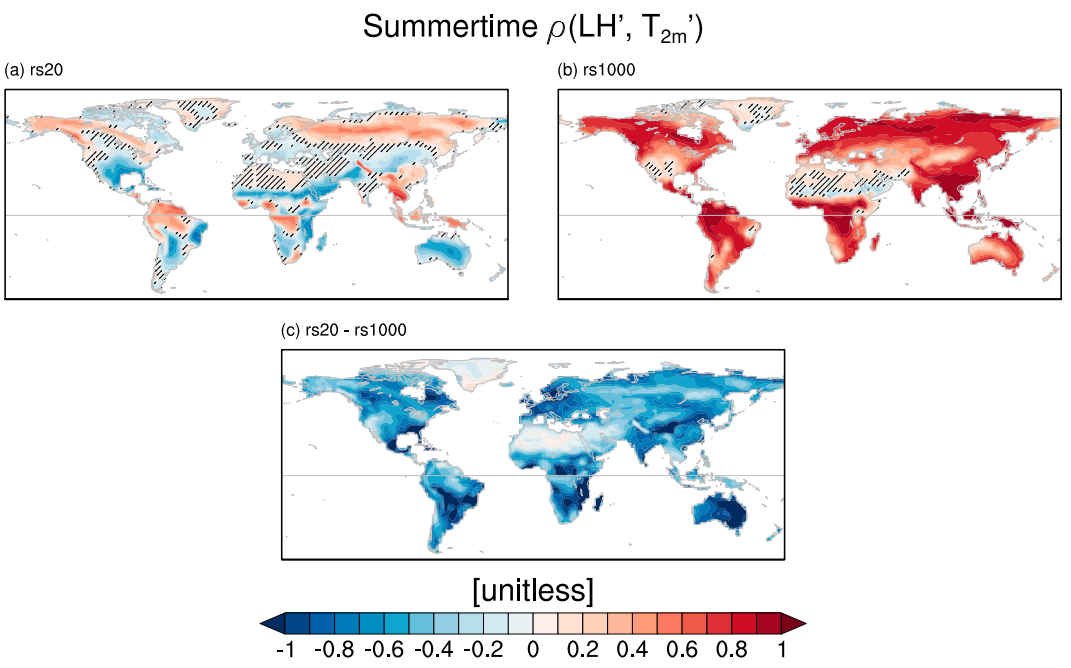

FIG. 5. Correlation between summer daily anomalies of latent heat flux (LH') and T_{2m}, denoted as $\rho(LH', T'_{2m})$, in (a) r_s20, (b) r_s1000, and (c) r_s20 minus r_s1000. Hatching in (a) and (b) indicates grid boxes that are not significant by applying a false discovery rate of 0.1 to p values calculated from a Student's t test. When estimating the degrees of freedom used for the p values calculation at each grid point in (a) and (b), we followed Eq. (3.4.2) of Bretherton (2014) by accounting for the lag-1 autocorrelation of summer daily LH′ and T'_{2m}.

of the influence of changes in advection is not negligible (Fig. S7).

d. *Changes in the land–atmosphere coupling*

We now explore how the land–atmosphere coupling responds to decreases in r_s. We examine changes in the correlation between summer daily anomalies of temperature and latent heat flux $\rho(\mathrm{LH}', T'_{2m})$, a measure of the soil moisture–temperature coupling strength (Lorenz et al. 2012; Seneviratne et al. 2006). Conceptually, the land surface in an energy-limited regime is primarily controlled by the atmosphere through radiation, thus positive $\rho(\mathrm{LH}', T'_{2m})$ usually implies an atmospheric controlled (energy-limited) regime. In contrast, negative $\rho(\mathrm{LH}', T'_{2m})$ often occurs in a soil-moisture controlled (water-limited) regime where a lack of soil moisture and evaporative cooling can amplify temperature anomalies (Schwingshackl et al. 2018; Zscheischler et al. 2015). In r_s20, T'_{2m} and LH′ are positively correlated in wet land areas such as the tropics and the high-latitude continental regions of the Northern Hemisphere, and negatively correlated in arid and transitional regions such as the southern United States, Australia, and interior Asia (Fig. 5a). In r_s1000, however, $\rho(\mathrm{LH}', T'_{2m})$ is positive nearly worldwide, although the positive correlation coefficients are small in arid and transitional areas, and the transitional Sahel region still shows a negative correlation (Fig. 5b). These results suggest that decreases in r_s reduce soil moisture amount in midlatitude land areas and lead these regions into a water-limited regime. In contrast, the tropical and high-latitude wet areas still stay in an energy-limited regime in the low r_s scenario, though the magnitude of $\rho(\mathrm{LH}', T'_{2m})$ decreases. Although the soil moisture–atmosphere interaction is present across our simulations, our high r_s case behaves somewhat analogously to the prescribed soil moisture simulation from the GLACE project, in which Berg et al. (2015) found that $\rho(\mathrm{LH}', T'_{2m})$ is globally positive because atmospheric evaporative demands (such as net radiation and temperature) rather than soil moisture availability drive the evapotranspiration and temperature variability when the soil moisture–atmosphere interaction is disabled. The primary reason that our high r_s case resembles Berg et al. (2015) is that large r_s makes it difficult for the land surface to evaporate water when there is available radiative energy at the surface, leading the soil moisture to remain ample; thus near-surface air temperature is less constrained by soil moisture availability.

We further demonstrate changes in the land surface evaporative regimes by examining the relationship between the summer mean evaporative fraction (EF) and soil moisture. EF is defined as the fraction of available energy partitioned toward latent heat fluxes: $\mathrm{EF} = \mathrm{LH}/(R_n - G) = \mathrm{LH}/(\mathrm{LH} + \mathrm{SH})$. Figure 6 presents the summer climatology of EF versus soil moisture from all grid points over land between 60°S and 60°N. Blue markers show results from r_s20, orange markers show r_s1000, and each marker indicates one grid point. Due to lower evaporative resistance, enhanced evaporative efficiency leads to higher EF in r_s20. The EF–soil moisture scatters distribution resembles the Budyko curve (Budyko 1961) and the conceptual framework proposed by Seneviratne et al. (2010).

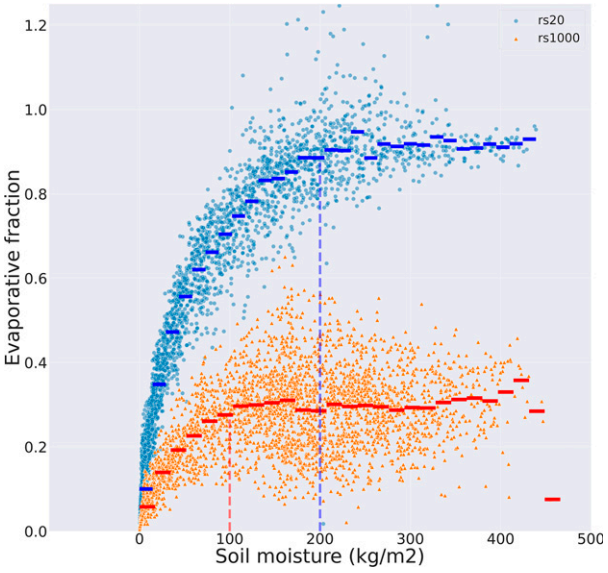

FIG. 6. Scatterplot of evaporative fraction (y axis) vs soil moisture (x axis). Results shown are summer climatology of land grid points in 60°S–60°N. Blue dot markers denote results from r_s20, and orange triangle markers denote results from r_s1000. The blue and red thick lines denote averaged evaporative fraction across grid points within each soil moisture bin (here, the binned average was implemented using the Python package scipy.stats.binned_statistic, with the number of equal-width bins set to 30). Vertical dashed lines indicate soil moisture thresholds separating water-limited regime (to the left of the dashed line) and energy-limited regime (to the right of the dashed line). These thresholds are obtained based on when the evaporative fraction–soil moisture slope becomes nearly zero. The blue dashed line at 200 kg m^{-2} is for r_s20, and the red dashed line at 100 kg m^{-2} is for r_s1000.

Across spatial grid points, in drier areas (water-limited regime), EF increases substantially at locations where the soil moisture is higher. In contrast, for wetter areas (energy-limited regime), EF is less sensitive to spatial variations in the soil moisture amount. Due to the low complexity of the bucket scheme for the hydrology, the dry regime (i.e., EF becomes zero where soil moisture is still available but is below the wilting point) does not exist in our simulations. The averaged EF values across soil moisture bins (denoted in the thick blue and red lines in Fig. 6) indicate a steeper EF–soil moisture slope in r_s20: EF exhibits a larger increase with increases in soil moisture across different regions, especially in water-limited areas. Based on the transition from a steep slope to a relatively flat slope, we use the vertical dashed lines in Fig. 6 as an estimated soil moisture threshold[5] for separating the water-limited and energy-limited regimes in each simulation. It suggests that the transition between an energy-limited and a water-limited regime happens at a higher soil moisture threshold in r_s20. Lower r_s makes it easier for the land surface to evaporate, therefore drier regions require a relatively high level of soil moisture to reach the condition when EF does not spatially vary with soil moisture; likewise, it is easier for a wetter region to transit into a water-limited regime in r_s20.

Taken together, a global decrease in r_s can shift the land area toward a more water-limited regime where temperature variability is more constrained by soil moisture availability. It is worth noting that the LH parameterization in SLIM is a simplification of reality, and the nonlinearity (i.e., the competing effects between r_s and β) built into the LH parameterization is important for us to understand changes in the land–atmosphere coupling in our simulations. On the one hand, the soil moisture amount becomes much lower in r_s20. On the other hand, small r_s itself implies stronger land–atmosphere coupling (i.e., a greater soil moisture control on evaporation) if soil moisture amount is identical between the high and low r_s cases. Further, the (admittedly large) perturbation in r_s could not only cause a shift in the land surface evaporative regimes but could also lead to a fundamental change in the structure of the relationship between soil moisture and EF (e.g., the EF-soil moisture slope) (Fig. 6). The narrative of future model projection studies usually emphasizes shifting from an energy-limited regime to a water-limited regime in some regions under global warming. For example, Seneviratne et al. (2006) found that increasing greenhouse gas concentrations makes central and eastern Europe a new transitional zone and consequently leads the area to experience enhanced temperature variability due to a stronger land–atmosphere coupling. Though we expect the effects of changes in r_s to be of second order compared to changes in the hydrological cycle under a changing climate, our finding suggests that future work investigating climatic forcing on land surface regimes should look beyond the regime shift by clarifying the potential changes in the steepness of the slope between EF and soil moisture.

4. Changes in the temperature variance Var(T'_{2m})

We now discuss the response of temperature variance to decreases in r_s, and the physical processes that cause the changes in the temperature variance. We find that decreasing r_s leads to an increase in Var(T'_{2m}) in drier areas such as the midlatitudes and a decrease in Var(T'_{2m}) in wetter areas such as the tropical and northern high latitudes (Fig. 7a). In the following, we will first seek to understand Var(T'_{2m}) changes through a surface energy budget perspective (section 4a). We will demonstrate that changes in the temperature variance can be largely explained by changes in the combined variance of SW and LH. We will then explore the effects of changes in the thermal advection variance, which appear to amplify changes in the temperature variance in the northern mid- to high latitudes (section 4b). We employ a multiple linear regression approach in section 4c to further discuss the relative importance of changes in the combined variance of SW and LH versus changes in the thermal advection variance on changes in the temperature variance. We end with a recap (section 4d) of lessons learned from this section.

[5] Note that the dashed line is a visual aid to roughly separate relatively wet and dry grid cells. The soil moisture threshold for separating water-limited and energy-limited areas might differ from the current study if the model used a different bucket fullness threshold that affects β.

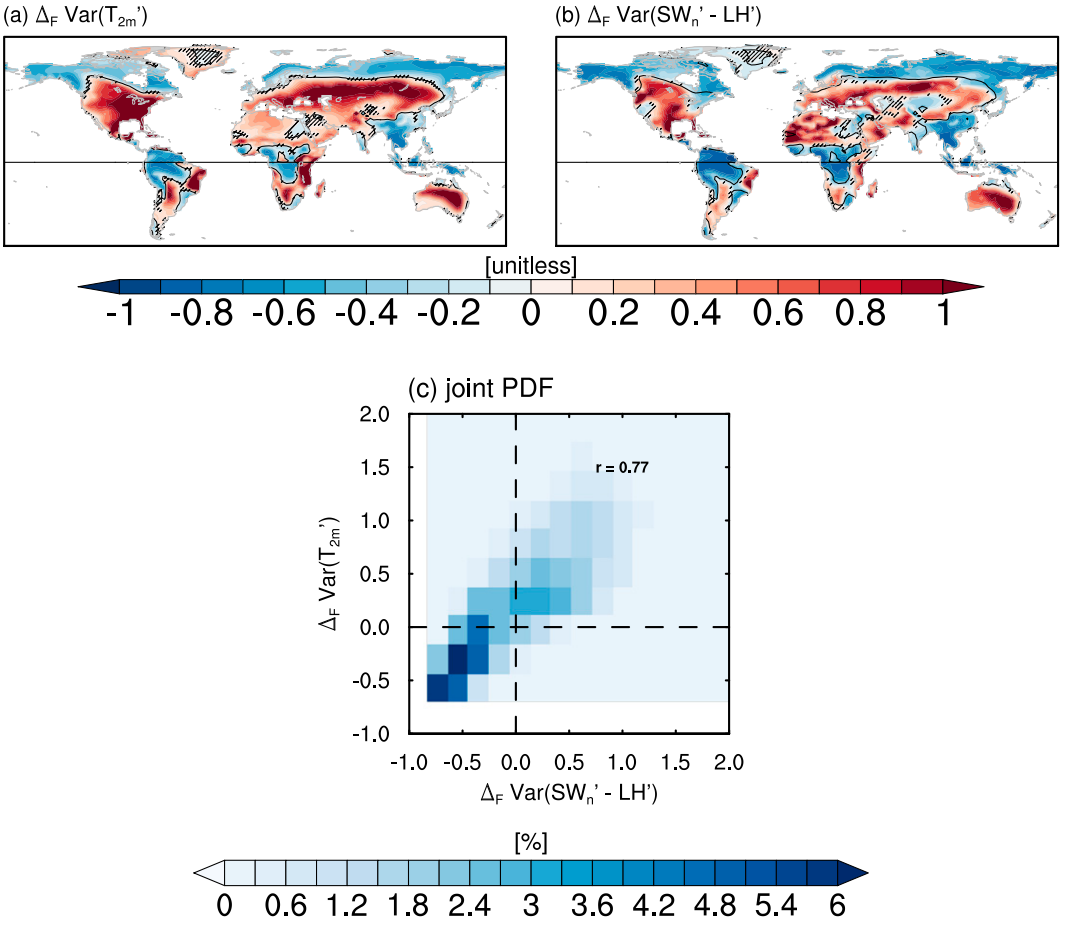

FIG. 7. The fractional changes [$\Delta_F = (r_s20 - r_s1000)/r_s1000$] in (a) the temperature variance and (b) combined variance of shortwave radiation and latent heat fluxes. Warm colors indicate an increase of variance, cold colors indicate a decrease of variance, and the black contour in (a) and (b) indicates the zero line of $\Delta_F \mathrm{Var}(T'_{2m})$ (c) The joint PDF (%) of $\Delta_F \mathrm{Var}(T'_{2m})$ in (a) against $\Delta_F \mathrm{Var}(\mathrm{SW}'_n - \mathrm{LH}')$ in (b) of all land grid points in 60°S–90°N excluding Greenland, in which the Pearson correlation coefficient is shown in the upper right corner.

a. *Linking changes of* $\mathrm{Var}(T'_{2m})$ *to changes in shortwave and latent heat fluxes*

Motivated by our earlier findings that changes in r_s can directly alter latent heat flux and indirectly alter incoming shortwave radiation through changes in cloudiness (section 3), we hypothesize that changes in the combined variance of shortwave and latent heat fluxes control the changes in the daily summer temperature variance as r_s decreases in the context of our simulations. Perturbations in the surface energy fluxes are directly linked to the surface (instead of near-surface) temperature, and previous studies suggest there could be discernible differences between responses of the 2-m air temperature and surface temperature to land surface perturbations at short time scales. For example, an observational study based in the southern Great Plains showed that compared to surface temperature, the response of 2-m temperature to changes in soil moisture is evidently weaker (Panwar et al. 2019). Despite this caveat, the near identical variance of near-surface air temperature and surface temperature in our simulations (see Fig. S8) suggest that it is a sound assumption to view near-surface and surface temperature as exchangeable in this context.

We rewrite the surface energy balance [Eq. (2)] in anomaly terms as

$$\mathrm{SW}'_n\downarrow - \mathrm{LH}'\uparrow = \mathrm{LW}'_n\uparrow + \mathrm{SH}'\uparrow + G'\downarrow, \qquad (3)$$

where on the left-hand side (LHS) we have grouped SW'_n and LH′ that have been clearly perturbed by the imposed r_s changes, and we thus view these two terms as forcing of changes in temperature variability in the context of our r_s perturbation simulations. We view the terms on the right-hand side (RHS) as the response to the forcing. We assume that LW'_n, SH′, and G' are all proportional to surface temperature in a quasi-linear fashion. Although the variation of ground heat flux could be complicated by landscape and the soil thermal properties (Purdy et al. 2016), an empirical linear relationship between the surface temperature and ground heat flux has been used to understand the global terrestrial surface energy budget (Mu et al. 2011). The sensible heat flux is proportional

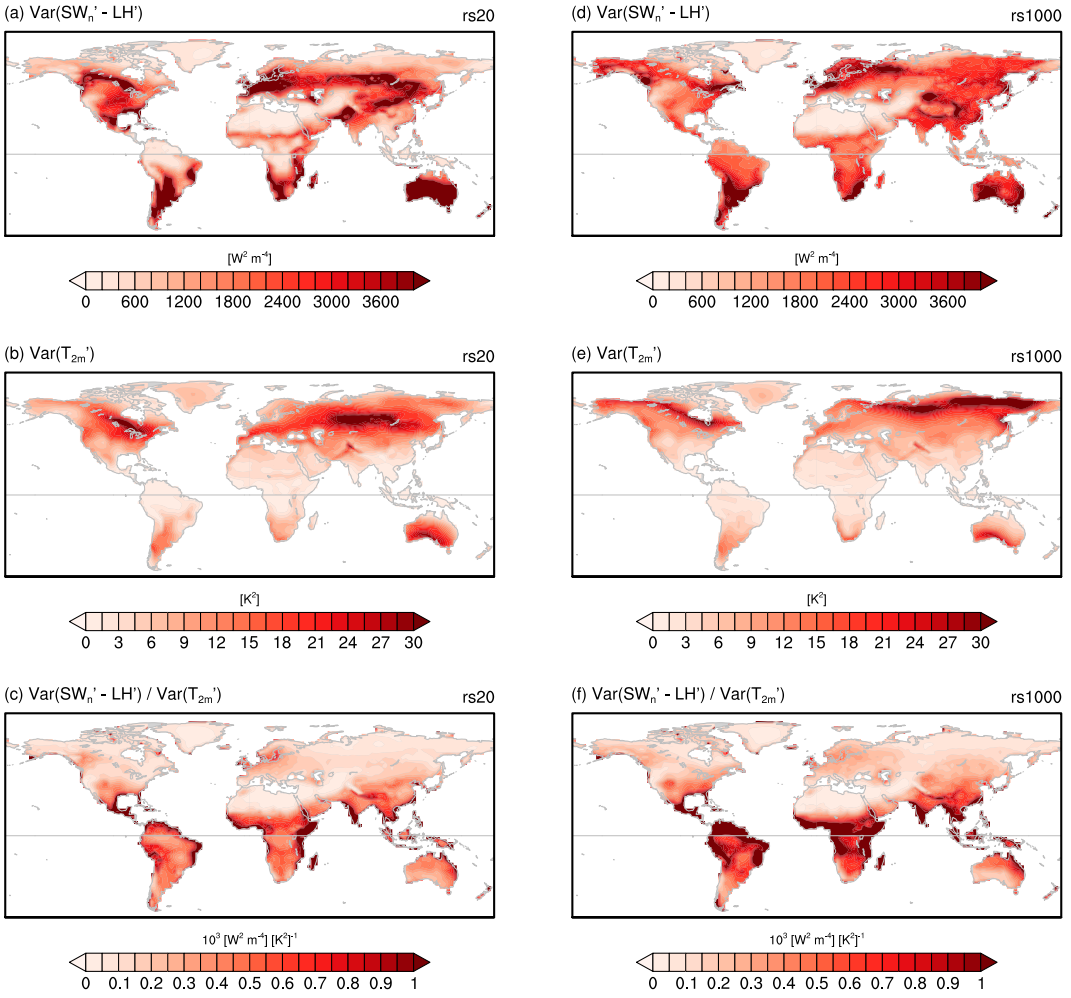

FIG. 8. (top) The combined variance of shortwave and latent heat flux $\mathrm{Var}(\mathrm{SW}'_n - \mathrm{LH}')$ in (a) r_s20 and (d) r_s1000. (middle) Temperature variance $\mathrm{Var}(T'_{2\mathrm{m}})$ in (b) r_s20 and (e) r_s1000. (bottom) Ratio of $\mathrm{Var}(\mathrm{SW}'_n - \mathrm{LH}')$ to $\mathrm{Var}(T'_{2\mathrm{m}})$ in (c) r_s20 and (f) r_s1000.

to the difference between the surface temperature and the near-surface air temperature: $\mathrm{SH} = \rho_{\mathrm{air}} C_p (T_s - T_a)/r_{ah}$, where ρ_{air} is the density of air (kg m^{-3}), C_p is the specific heat constant (J kg^{-1} K^{-1}), T_a is the near-surface air temperature (K) (in CESM, atmospheric temperature at the lowest model level is used to represent T_a; Collins et al. 2004), and r_{ah} is the aerodynamic resistance (s m^{-1}). Therefore, it is reasonable to expect a linear relationship between SH and T_s if $\rho_{\mathrm{air}} C_p / r_{ah}$ does not vary substantially and T_a is proportional to T_s by a factor that does not vary substantially. LW_u is approximated as a linear function of surface temperature via implicit linearization of the Plank feedback, and LW_d is assumed to vary linearly with temperature due to the close coupling between LW'_d and the near-surface temperature. In agreement with these assumptions, changes in the variability of the longwave, sensible heat, and ground heat flux (see Fig. S9) indeed resemble the pattern of the temperature variability change, suggesting that variations of surface temperature are closely related to the variations of the energy flux terms on the RHS of Eq. (3).

If our proposed framework of viewing changes in $\mathrm{Var}(\mathrm{SW}'_n - \mathrm{LH}')$ as the forcing and viewing changes in $\mathrm{Var}(T'_{2\mathrm{m}})$ as the response is valid, we should expect that regions experiencing enhanced $\mathrm{Var}(\mathrm{SW}'_n - \mathrm{LH}')$ to exhibit an increase in $\mathrm{Var}(T'_{2\mathrm{m}})$ and that regions with reduced $\mathrm{Var}(\mathrm{SW}'_n - \mathrm{LH}')$ show a decrease in $\mathrm{Var}(T'_{2\mathrm{m}})$. Here, we use the fractional difference [denoted as Δ_F; $\Delta_F = (r_s20 - r_s1000)/r_s1000$] instead of the actual difference ($\Delta = r_s20 - r_s1000$) to test the causal linkage between changes in $\mathrm{Var}(\mathrm{SW}'_n - \mathrm{LH}')$ and changes in $\mathrm{Var}(T'_{2\mathrm{m}})$ on a global scale. Our motivation for using the fractional difference is as follows. We assume $\mathrm{Var}(T'_{2\mathrm{m}})$ is linked to $\mathrm{Var}(\mathrm{SW}'_n - \mathrm{LH}')$ as $\mathrm{Var}(\mathrm{SW}'_n - \mathrm{LH}') \sim \alpha\, \mathrm{Var}(T'_{2\mathrm{m}})$, where α can be understood as a measure of the sensitivity of $\mathrm{Var}(T'_{2\mathrm{m}})$ against $\mathrm{Var}(\mathrm{SW}'_n - \mathrm{LH}')$ at each grid point. We present $\mathrm{Var}(\mathrm{SW}'_n - \mathrm{LH}')$, $\mathrm{Var}(T'_{2\mathrm{m}})$, and α from each simulation in Fig. 8. As expected, α varies spatially due to the spatial heterogeneity in a number of processes linking surface fluxes to temperature (Figs. 8c,f). Therefore, comparing changes in $\mathrm{Var}(\mathrm{SW}'_n - \mathrm{LH}')$ and $\mathrm{Var}(T'_{2\mathrm{m}})$ across a global scale using the

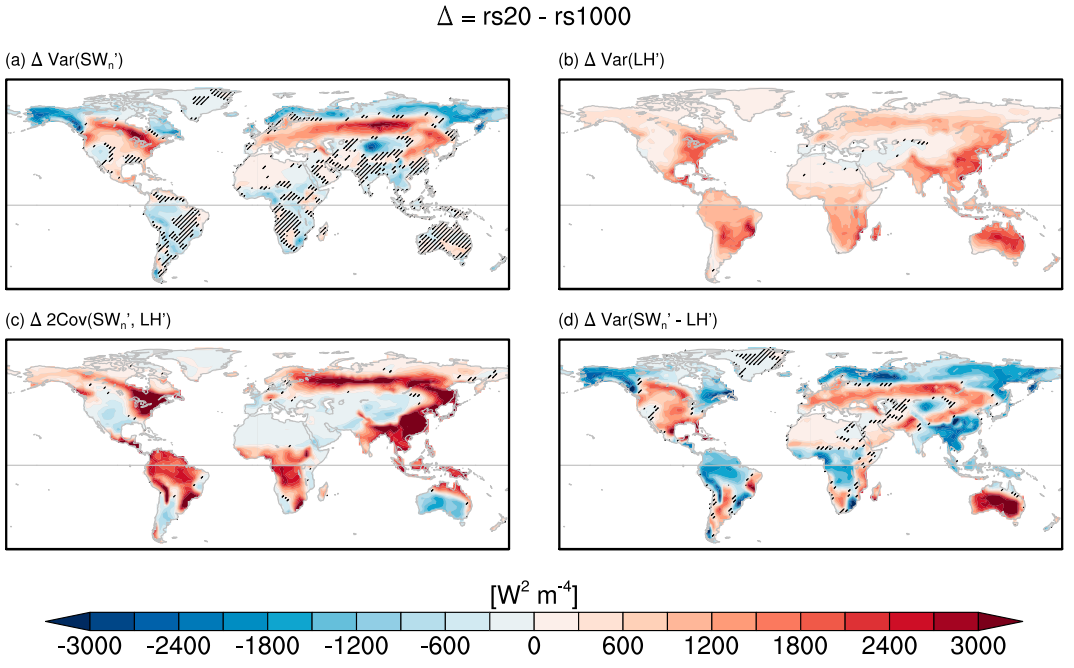

FIG. 9. Changes ($r_s20 - r_s1000$) in (a) variance of shortwave radiation, (b) variance of latent heat flux, (c) covariance of shortwave radiation and latent heat flux, and (d) combined variance of shortwave radiation and latent heat flux. Note that (d) is the same as Fig. 7b except that Fig. 7b shows the fractional change of variance.

actual difference will be complicated by the fact that the sensitivity of $\mathrm{Var}(T'_{2\mathrm{m}})$ against $\mathrm{Var}(\mathrm{SW}'_n - \mathrm{LH}')$ varies spatially. Note that despite the significant responses of both $\mathrm{Var}(\mathrm{SW}'_n - \mathrm{LH}')$ and $\mathrm{Var}(T'_{2\mathrm{m}})$ to decreasing r_s, α exhibits a strong resemblance between the two simulations (the centered pattern correlation between Figs. 8c and 8f is 0.85). Our speculation is that this is likely because α primarily depends on the soil type and soil thermal properties at the land surface, and these surface properties are prescribed and kept the same between the two simulations. We thus assume that the spatial variation in the sensitivity of $\mathrm{Var}(T'_{2\mathrm{m}})$ against $\mathrm{Var}(\mathrm{SW}'_n - \mathrm{LH}')$ is exchangeable between r_s20 and r_s1000, and we can write out the comparison between the fractional difference of $\mathrm{Var}(T'_{2\mathrm{m}})$ and $\mathrm{Var}(\mathrm{SW}'_n - \mathrm{LH}')$ at each grid point as follows: $\Delta_F\mathrm{Var}(T'_{2\mathrm{m}})/[\Delta_F\mathrm{Var}(\mathrm{SW}'_n - \mathrm{LH}')] \sim \{\Delta\mathrm{Var}(T'_{2\mathrm{m}})/[\Delta\mathrm{Var}(\mathrm{SW}'_n - \mathrm{LH}')]\} \times \alpha$. Therefore, using the fractional difference helps to put changes in $\mathrm{Var}(T'_{2\mathrm{m}})$ and changes in $\mathrm{Var}(\mathrm{SW}'_n - \mathrm{LH}')$ at different locations on the same footing by removing the spatial variation in the sensitivity of $\mathrm{Var}(T'_{2\mathrm{m}})$ to $\mathrm{Var}(\mathrm{SW}'_n - \mathrm{LH}')$ and allows us to assess the linkage between changes in $\mathrm{Var}(T'_{2\mathrm{m}})$ and changes in $\mathrm{Var}(\mathrm{SW}'_n - \mathrm{LH}')$ across the global land area in a more quantitative manner. It is interesting to note that $\mathrm{Var}(\mathrm{SW}'_n - \mathrm{LH}')$ and $\mathrm{Var}(T'_{2\mathrm{m}})$ do not closely align with each other within each separate simulation (Figs. 8a,b,d,e), which is likely due to the spatial variation in α.

As expected, the spatial maps of $\Delta_F\mathrm{Var}(\mathrm{SW}'_n - \mathrm{LH}')$ and $\Delta_F\mathrm{Var}(T'_{2\mathrm{m}})$ closely resemble each other (Figs. 7a,b): both show a reduced variability in the tropics and the northern high latitudes and an enhanced variability in the extratropical land areas in the low r_s case. The joint probability density function (PDF) of $\Delta_F\mathrm{Var}(T'_{2\mathrm{m}})$ versus $\Delta_F\mathrm{Var}(\mathrm{SW}'_n - \mathrm{LH}')$ using land grid points between 60°S and 90°N excluding Greenland from Figs. 7a and 7b further suggests that $\Delta_F\mathrm{Var}(T'_{2\mathrm{m}})$ vary with $\Delta_F\mathrm{Var}(\mathrm{SW}'_n - \mathrm{LH}')$ in a quasi-linear fashion, with a spatial-cross correlation of 0.77 (Fig. 7c).

We now expand the combined variance of the LHS of Eq. (3) as

$$\mathrm{Var}(\mathrm{SW}'_n - \mathrm{LH}') = \mathrm{Var}(\mathrm{SW}'_n) + \mathrm{Var}(\mathrm{LH}') - 2 \times \mathrm{Cov}(\mathrm{SW}'_n, \mathrm{LH}') \quad (4)$$

and discuss changes in the variability of shortwave and latent heat flux, as well as changes in their covariance, and how these changes contribute to the changes in their combined variance (Fig. 9). Changes in $\mathrm{Var}(\mathrm{SW}'_n)$ are most pronounced in the Northern Hemisphere, while the Southern Hemisphere shows minimal difference between the two simulations (Fig. 9a). Changes in $\mathrm{Var}(\mathrm{SW}'_n)$ are primarily controlled by perturbations in the variability of cloud cover, which is closely coupled with the vertical distribution of temperature and moisture, and the atmospheric boundary layer structure (Klein 1997; Norris 1998). Indeed, $\mathrm{Var}(\mathrm{SW}'_n)$ under clear sky is nearly identical between the high and low r_s cases (Fig. S9a), indicating that changes in the cloudiness are the root cause of the shortwave variability change. Variations in low clouds are most effective in affecting the shortwave radiation as low clouds are almost opaque to the shortwave. Like changes in $\mathrm{Var}(\mathrm{SW}'_n)$, changes in the variability of the low cloud cover are especially pronounced in the Northern Hemisphere mid-to-high latitudes, where the low cloud cover exhibits reduced variability in the polar region and enhanced variability in the midlatitudes (see Fig. S10b). These changes in the low cloud cover variability

can be linked to the low cloud cover in the mean state, which presents a cloudier condition in the high latitudes and is less cloudy in the mid latitudes. Since the low cloud cover increases everywhere when r_s decreases (Fig. 3c), its variance in regions where it is already very cloudy is reduced because the cloud fraction cannot become greater than one and the increased cloud fraction means that less cloudy days are less likely. In less cloudy regions, however, increasing cloud fraction increases the variance because the probability of having cloudier days in those areas increases. Var(LH′) increases in most land areas in r_s20 (Fig. 9b) due to the enhanced evaporation efficiency (Fig. 6). Regions that experienced an increase in summer mean latent heat flux exhibit an enhancement of Var(LH′). It is worth noting that although the latent heat flux enhancement peaks in the tropics, the magnitude of the Var(LH′) enhancement is largest over extratropical land areas. In contrast, there is a slight decrease in Var(LH′) over regions that experienced a reduction of latent heat in the summer mean state (Fig. 2h), such as the west to central United States, North Africa, and interior Asia. Soil moisture in these regions becomes critically low in r_s20 and limits further evaporation and reduces Var(LH′). Though being a relatively wet area, the magnitude of the Var(LH′) changes in the Northern Hemisphere high latitudes is small, which is likely due to the reduced shortwave variance in the region (cf. Figs. 9a,b). Compared to r_s1000, the covariance of shortwave and latent heat flux increases in wetter areas and decreases in drier areas in r_s20 (Fig. 9c). Assuming the same magnitude of positive shortwave anomalies in both scenarios, more positive evaporation anomalies can occur over wet land surface in the low r_s case due to the low resistance to evaporation. In contrast, less evaporation would occur over dry land surface in the low r_s case because of the limited soil moisture availability. Interestingly, the joint PDF between $\Delta\mathrm{Var}(T'_{2\mathrm{m}})$ and $\Delta\mathrm{Var}(\mathrm{SW}'_n - \mathrm{LH}')$ (Fig. 7c) suggests that an enhancement of $\mathrm{Var}(T'_{2\mathrm{m}})$ could occur even when $\Delta\mathrm{Var}(\mathrm{SW}'_n - \mathrm{LH}')$ is negative or zero, suggesting that other factors may contribute to changes in temperature variance in some regions.

b. *Changes in the variance of thermal advection*

We now explore the effects of horizontal thermal advection on the variation of near-surface air temperature. We obtain daily anomalies of thermal advection by removing the seasonal cycle (i.e., the first 10 harmonics of the daily climatology) of $-\mathbf{u}\cdot\nabla T$, that is,[6] $-(\mathbf{u}\cdot\nabla T)' = (-\mathbf{u}\cdot\nabla T) - \overline{(-\mathbf{u}\cdot\nabla T)}$, where $\overline{(\cdot)}$ denotes climatology, and $(\cdot)'$ denotes an anomaly. In the following, we denote daily anomalies of thermal advection at the lowest atmospheric model level as advTBOT′. Analysis using the 850-hPa thermal advection gives similar results (not shown).

The strong resemblance between changes in the thermal advection variance (Fig. 10a) and changes in temperature variance (Fig. 7a) in the northern mid- to high latitudes suggests that besides the combined variance of shortwave radiation and latent heat flux, thermal advection may also play a role in shaping the extratropical temperature variance response to decreasing r_s. However, the overall correspondence between changes in the temperature variance and thermal advection variance is less clear-cut than changes in $\mathrm{Var}(\mathrm{SW}'_n - \mathrm{LH}')$. The spatial cross-correlation coefficient between the fractional change of variance is 0.43 for $\Delta_F\mathrm{Var}(T'_{2\mathrm{m}})$ and $\Delta_F\mathrm{Var}(\mathrm{advTBOT}')$, smaller than the correlation between $\Delta_F\mathrm{Var}(T'_{2\mathrm{m}})$ and $\Delta_F\mathrm{Var}(\mathrm{SW}'_n - \mathrm{LH}')$ (section 4a and Fig. 7c), which is 0.77. The latitudinal correlation between the fractional changes of variance (Fig. 10b) further demonstrates a stronger connection between $\Delta_F\mathrm{Var}(\mathrm{SW}'_n - \mathrm{LH}')$ and $\Delta_F\mathrm{Var}(T'_{2\mathrm{m}})$ across all latitudes. In contrast, the effects of $\Delta_F\mathrm{Var}(\mathrm{advTBOT}')$ are most pronounced in the northern mid- to high latitudes but are weaker in austral summer and the tropics.

c. *Reconstruction of temperature variability using multiple linear regression (MLR)*

To quantify the relative importance of $(\mathrm{SW}'_n - \mathrm{LH}')$ and advTBOT′ in the magnitude of changes in $\mathrm{Var}(T'_{2\mathrm{m}})$, we construct a multiple linear regression (MLR) model for $T'_{2\mathrm{m}}$, at each grid point, as follows:

$$T'_{2\mathrm{m}} = b_0 + b_1(\mathrm{SW}'_n - \mathrm{LH}') + b_2(\mathrm{advTBO}T') + \epsilon, \qquad (5)$$

where b_0 denotes the intercept, b_1 and b_2 denote the regression coefficients, and E denotes the residual. To solely focus on the effects of changes in the variance of $(\mathrm{SW}'_n - \mathrm{LH}')$ and advTBOT′, we assume that there is no change in b_0, b_1, and b_2 between the two simulations. That is, r_s20 and r_s1000 share the same MLR model. To this end, we construct the MLR model using $T'_{2\mathrm{m}}$, $(\mathrm{SW}'_n - \mathrm{LH}')$, and advTBOT′ that are concatenated from r_s20 and r_s1000 together.

Based on the proposed MLR model, we reconstruct the $T'_{2\mathrm{m}}$ variance explained by $(\mathrm{SW}'_n - \mathrm{LH}')$ and advTBOT′ in each simulation [denoted as $\mathrm{Var}(T'_{2\mathrm{m}})_{\mathrm{MLR}}$] as follows:

$$\mathrm{Var}(T'_{2\mathrm{m}})_{\mathrm{MLR}} = b_1^2\mathrm{Var}(\mathrm{SW}'_n - \mathrm{LH}') + b_2^2\mathrm{Var}(\mathrm{advTBOT}') + 2b_1b_2\mathrm{Cov}(\mathrm{SW}'_n - \mathrm{LH}', \mathrm{advTBOT}'), \qquad (6)$$

where we use $\mathrm{Var}(\mathrm{SW}'_n - \mathrm{LH}')$, $\mathrm{Var}(\mathrm{advTBOT}')$, and $\mathrm{Cov}(\mathrm{SW}'_n - \mathrm{LH}', \mathrm{advTBOT}')$ from each separate simulation to calculate $\mathrm{Var}(T'_{2\mathrm{m}})_{\mathrm{MLR}}$ in r_s20 and r_s1000, while the regression coefficients b_1 and b_2 (Fig. 11) stay the same. Spatial patterns of $\mathrm{Var}(T'_{2\mathrm{m}})_{\mathrm{MLR}}$ (Figs. S11a,e) closely resemble the actual $T'_{2\mathrm{m}}$ variance in each simulation (Figs. 8b,e). As expected, the magnitude of $\mathrm{Var}(T'_{2\mathrm{m}})_{\mathrm{MLR}}$ (Figs. S11a,e) is smaller than the actual $T'_{2\mathrm{m}}$ variance. This is likely due to the regression dilution bias (Hutcheon et al. 2010) as well as the fact that we are only considering effects of $(\mathrm{SW}'_n - \mathrm{LH}')$ and advTBOT′. Most of the MLR reconstructed $T'_{2\mathrm{m}}$ variance comes from $b_1^2\mathrm{Var}(\mathrm{SW}'_n - \mathrm{LH}')$, with the contribution from $b_2^2\mathrm{Var}(\mathrm{advTBOT}')$ being secondary and concentrating over extratropical land area (Fig. S11). We further explore contributions of each process from the RHS of Eq. (6) to changes

[6] Some authors (e.g., Holmes et al. 2016) have directly used $-\mathbf{u}'\cdot\overline{T}$ to represent thermal advection anomalies, thereby assuming that advection across climatological temperature gradients by the anomalous wind dominates changes in the advection. Results based on this calculation approach are consistent with those reported here.

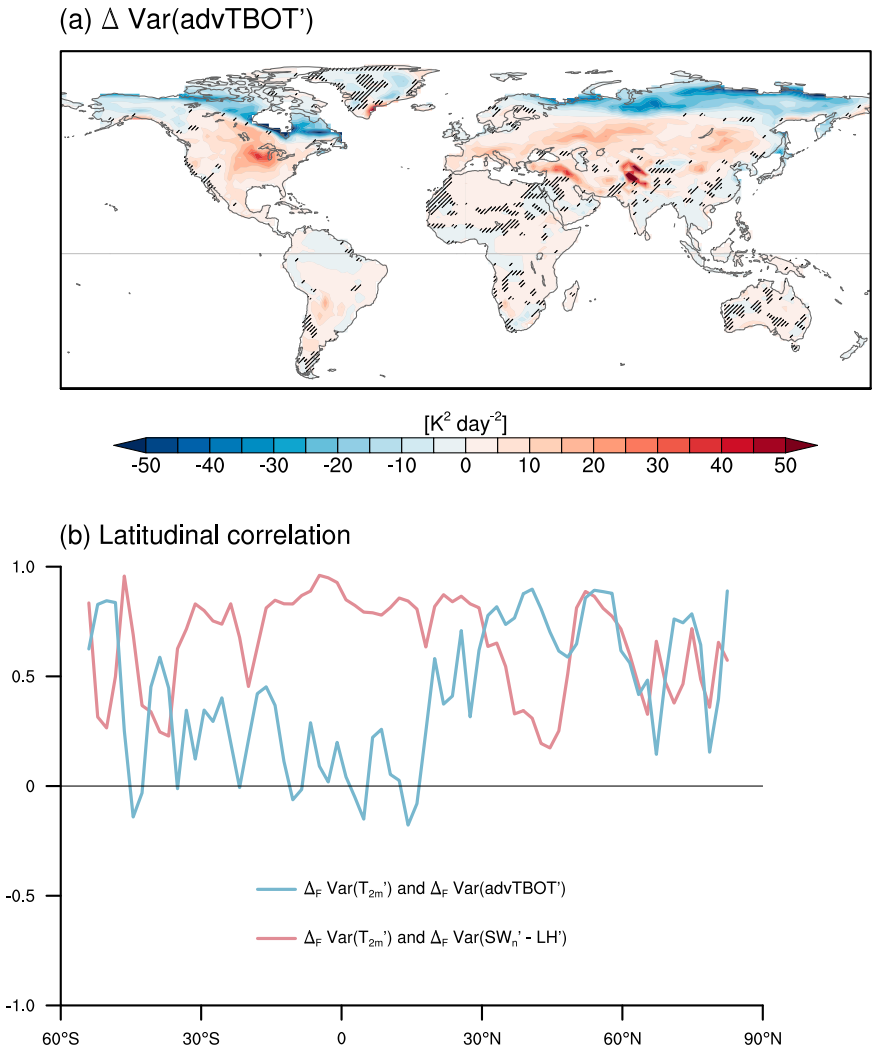

FIG. 10. (a) Changes ($\Delta = r_s20 - r_s1000$) in the variance of thermal advection (K^2 day^{-2}) at the lowest atmospheric model level. (b) Latitudinal correlations across the fractional change [$\Delta F = (r_s20 - r_s1000)/r_s1000$] of variances, between $\Delta_F \mathrm{Var}(T'_{2m})$ and $\Delta_F \mathrm{Var}(\mathrm{SW}'_n - \mathrm{LH}')$ in pink, and between $\Delta_F \mathrm{Var}(T'_{2m})$ and Δ_FVar(advTBOT') in blue. Correlations were calculated from land grid points across longitude at each latitude between 60°S and 90°N, excluding Greenland.

($\Delta = r_s20 - r_s1000$) in the MLR reconstructed T'_{2m} variance (Figs. 12a–d). It suggests that changes in $\mathrm{Var}(T'_{2m})_{MLR}$ (Fig. 12d) are primarily due to changes in T'_{2m} variance reconstructed from $\mathrm{Var}(\mathrm{SW}'_n - \mathrm{LH}')$ and the regression coefficients b_1 (Fig. 12a). In contrast, changes in T'_{2m} variance reconstructed from Var(advTBOT′) and the regression coefficients b_2 are only pronounced in northern mid- to high latitudes (Fig. 12b). Note that accounting for changes in Var(advTBOT′) resolves some of the mismatches between changes in $\mathrm{Var}(T'_{2m})$ and changes in $\mathrm{Var}(\mathrm{SW}'_n - \mathrm{LH}')$ such as that over southeastern Canada, where $\mathrm{Var}(\mathrm{SW}'_n - \mathrm{LH}')$ decreases while $\mathrm{Var}(T'_{2m})$ increases. Figures 12d–f further demonstrate that changes in T'_{2m} variance reconstructed from the MLR model captured the actual changes in T'_{2m} variance reasonably well, with the joint PDF between $\Delta\mathrm{Var}(T'_{2m})_{MLR}$ and $\Delta\mathrm{Var}(T'_{2m})$ land grid points in 60°S–90°N (excluding Greenland) exhibits a strong linear relationship (the Pearson correlation coefficient is 0.8).

Our MLR analysis support our earlier interpretation that changes in $\mathrm{Var}(T'_{2m})$ can be primarily explained by changes in $\mathrm{Var}(\mathrm{SW}'_n - \mathrm{LH}')$ across a global scale, while changes in Var(advTBOT′) mainly affect the northern mid- to high latitudes. Still, we should note the caveat of our assumption that r_s20 and r_s1000 share the same regression coefficients, because there are several areas in the northern extratropical land area where the regression coefficients exhibit evident differences between r_s20 and r_s1000 (not shown). Understanding changes in the regression coefficients of T'_{2m} onto its physical drivers could be important for accurately predicting the magnitude of responses in T'_{2m} variance to land surface forcing. However, it is beyond the scope of our current study, and we leave that exploration for future investigations.

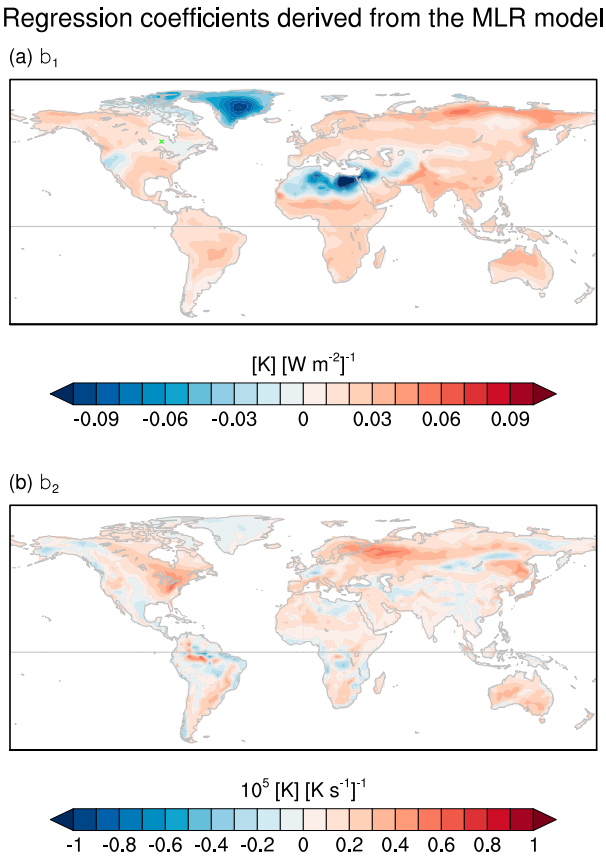

FIG. 11. Regression coefficients derived from the MLR model: (a) b_1 [K (W m^{-2})$^{-1}$] and (b) b_2 [K (K s^{-1})$^{-1}$].

d. Recap

We provide an overview of this section's main message in Fig. 13. Figures 13a–d compare r_s20 and r_s1000 simulated distribution of T'_{2m}, $SW'_n - LH'$, and advTBOT′ (similar results are found for advT850′; not shown) over several representative locations spanning different latitudes that either experienced an increase or a decrease of temperature variance. The U.S. Midwest (Fig. 13a) and Australia (Fig. 13b) points are typical extratropical land areas from boreal summer and austral summer, respectively. Both locations experience an increase in temperature variance when r_s decreases, as demonstrated by the wider range of T'_{2m} simulated in r_s20. The increase of $\mathrm{Var}(T'_{2m})$ in the U.S. Midwest can be attributed to an increase in both $\mathrm{Var}(SW'_n - LH')$ and $\mathrm{Var}(\mathrm{advTBOT}')$. In contrast, the increase of $\mathrm{Var}(T'_{2m})$ in Australia is mainly due to the enhanced $\mathrm{Var}(SW'_n - LH')$. The decrease in $\mathrm{Var}(T'_{2m})$ in r_s20 at the Amazon point, which is representative of the tropical land areas, is due to decreases in $\mathrm{Var}(SW'_n - LH')$ in the region (Fig. 13c). For Siberia, which is representative of northern high latitudes, both decreases in $\mathrm{Var}(SW'_n - LH')$ and $\mathrm{Var}(\mathrm{advTBOT}')$ contribute to decreases in $\mathrm{Var}(T'_{2m})$ (Fig. 13d).

Taken together, the response of summer continental temperature variance to the r_s perturbations in our simulations can be explained to first order by changes in the combined variance of shortwave and latent heat fluxes. We think this is a valid framework because, compared to other surface energy fluxes, shortwave radiation and latent heat flux are more directly influenced by the r_s perturbations. Therefore, by viewing $\Delta_F\mathrm{Var}(SW'_n - LH')$ as the forcing of the surface energy budget and by viewing $\Delta_F\mathrm{Var}(T'_{2m})$ as the response, we find a largely coherent change between the two quantities (Figs. 13e,f). It is worth noting that the spatial pattern of $\Delta_F\mathrm{Var}(T'_{2m})$ resembles the spatial patterns of summer soil moisture climatology (see Fig. 1) and changes in the covariance between SW'_n and LH′ (see Fig. 9c). Reducing r_s leads climatologically drier areas to become more water-limited, which reduces $\mathrm{Cov}(SW'_n, LH')$, thus weakening the damping effect of evaporative cooling and enhancing $\mathrm{Var}(T'_{2m})$. In contrast, climatologically wetter areas experience an increase of $\mathrm{Cov}(SW'_n, LH')$, and thus a decrease in $\mathrm{Var}(T'_{2m})$. Further analysis suggests that changes in the horizontal thermal advection variance also act to shape the temperature variance response, especially in the northern mid- to high latitudes (Fig. 13g). Note that neither $\Delta_F\mathrm{Var}(SW'_n - LH')$ nor $\Delta_F\mathrm{Var}(\mathrm{advTBOT}')$ provides a satisfactory explanation for $\Delta_F\mathrm{Var}(T'_{2m})$ in some regions, such as the southwestern United States. Such discrepancies suggest that other possible drivers (such as downwelling longwave radiation and vertical motion) of temperature variance change should be taken into account when assessing the effects of land surface perturbations on local scales. Further, changes in the sensitivity of T'_{2m} to $(SW'_n - LH')$ and advTBOT′ could be important in understanding the magnitude of changes in $\mathrm{Var}(T'_{2m})$ in some regions.

5. Discussion

Our diagnostic framework of using the combined variance of shortwave and latent heat flux to understand changes in summer temperature variance bears similarities with previous studies (Gregory and Mitchell 1995; Vargas Zeppetello et al. 2020). Gregory and Mitchell (1995) examined changes of summer daily surface temperature variance over Europe in the equilibrium climate with a doubled atmospheric concentration of carbon dioxide. They found that in a warming climate, changes in the temperature variance are closely related to changes in the ratio of latent heat flux to the sum of land surface turbulent heat and net longwave fluxes [λ, hereafter; $\lambda = \mathrm{LH}\uparrow/(\mathrm{LH}\uparrow + \mathrm{SH}\uparrow + \mathrm{LW}_n\uparrow) = \mathrm{LH}\uparrow/(\mathrm{SW}\downarrow + G\downarrow)$]. That is, daily temperature variance increases when λ decreases, and temperature variance decreases when λ increases. The magnitude of λ reflects the background soil moisture availability, which, as discussed above, can affect the temperature variance by modulating the portion of net radiation used for evaporation. For example, when soil moisture is ample, a larger portion of net radiative energy anomalies is associated with altered evaporation of water from the land surface and thus a smaller portion warms up the land surface, resulting in reduced temperature variability. We examined the summer climatology of λ in both simulations and found that

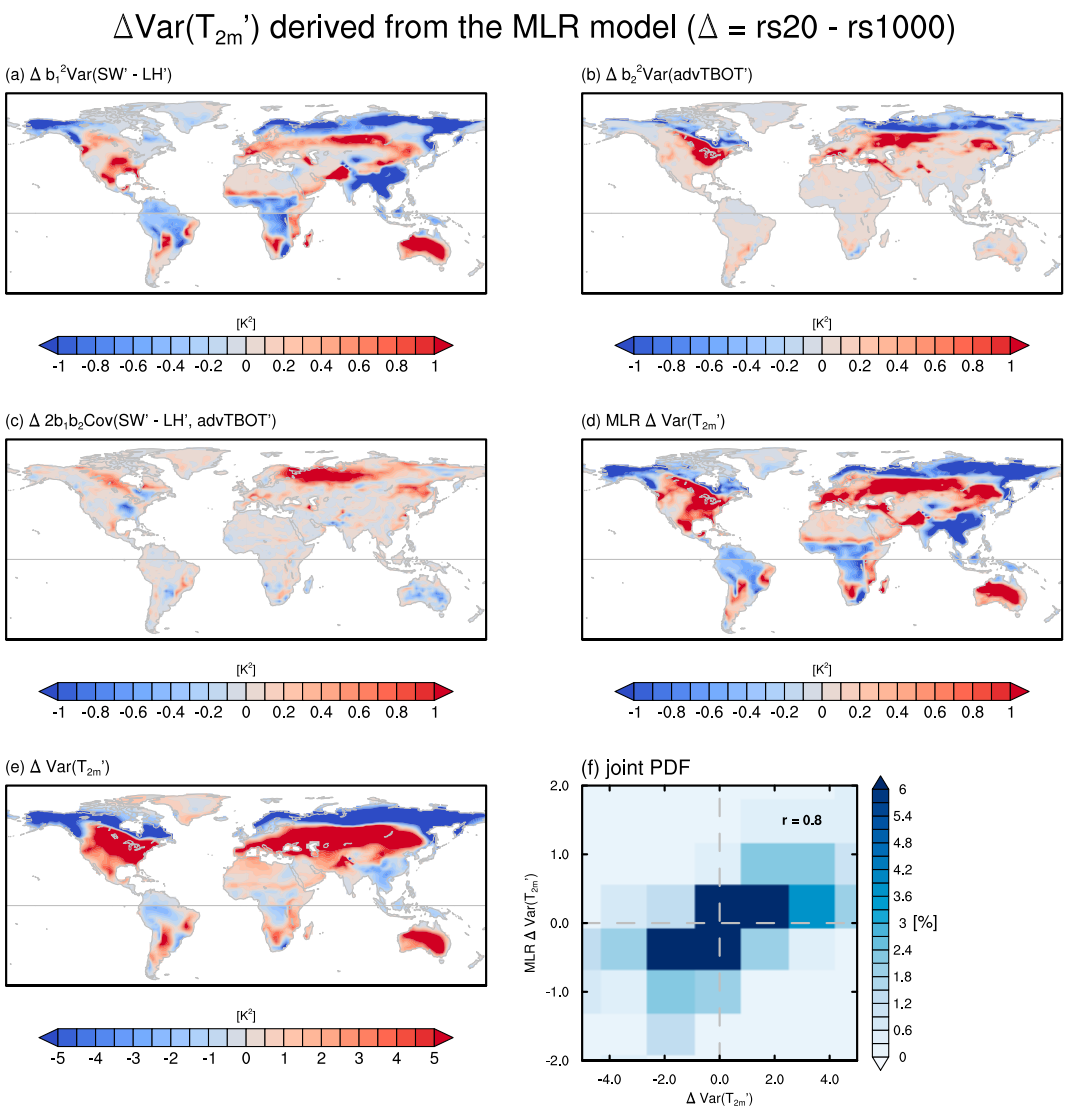

FIG. 12. Changes ($\Delta = r_s20 - r_s1000$) in the multiple linear regression (MLR) reconstructed $\mathrm{Var}(T'_{2\mathrm{m}})$ Shown are $\Delta\mathrm{Var}(T'_{2\mathrm{m}})$ due to (a) changes in $b_1^2\mathrm{Var}(\mathrm{SW}'_n - \mathrm{LH}')$, (b) changes in $b_2^2\mathrm{Var}(\mathrm{advTBOT}')$, and (c) changes in $2b_1b_2\,\mathrm{Cov}(\mathrm{SW}'_n - \mathrm{LH}', \mathrm{advTBOT}')$ (d) Total MLR reconstructed $\Delta\mathrm{Var}(T'_{2\mathrm{m}})$ from the sum of (a) to (c), and (e) $\Delta\mathrm{Var}(T'_{2\mathrm{m}})$ directly calculated from $T'_{2\mathrm{m}}$ in each simulation. (f) The joint PDF (%) of $\Delta\mathrm{Var}(T'_{2\mathrm{m}})_{\mathrm{MLR}}$ in (d) against $\Delta\mathrm{Var}(T'_{2\mathrm{m}})$ in (e) of all land grid points between 60°S and 90°N (excluding Greenland), with the Pearson correlation coefficient shown in the upper right corner.

regions with more ample background soil moisture indeed present a larger evaporative cooling ratio (see Fig. S12). In agreement with Gregory and Mitchell (1995), we found an overall negative relationship between changes in temperature variance and changes in λ: the correlation coefficient of these values over land grid points between 60°S and 90°N excluding Greenland is −0.5. The fact that changes in $\mathrm{Var}(\mathrm{SW}'_n - \mathrm{LH}')$ yield a stronger magnitude of correlation ($r = 0.77$; see section 4a) with changes in temperature variance suggests that our approach is more accurate in understanding the response of summer daily temperature variance to the r_s perturbations, likely because we explicitly consider how changes in the variances of the energy budget terms would be expected to link to changes in temperature variance.

A similar framework was developed by Vargas Zeppetello et al. (2020). Based on the surface energy and water budget, they found that summer monthly temperature variance in the mean state can be modeled as a linear response to combined variance of shortwave radiation and precipitation anomalies. Vargas Zeppetello and Battisti (2020) further employed that framework to explore the sensitivity of summer monthly temperature variance to surface warming due to increasing carbon dioxide. Our framework is distinct in that we view the latent heat flux (in response to perturbations in the land surface properties) rather than precipitation as a forcing variable,

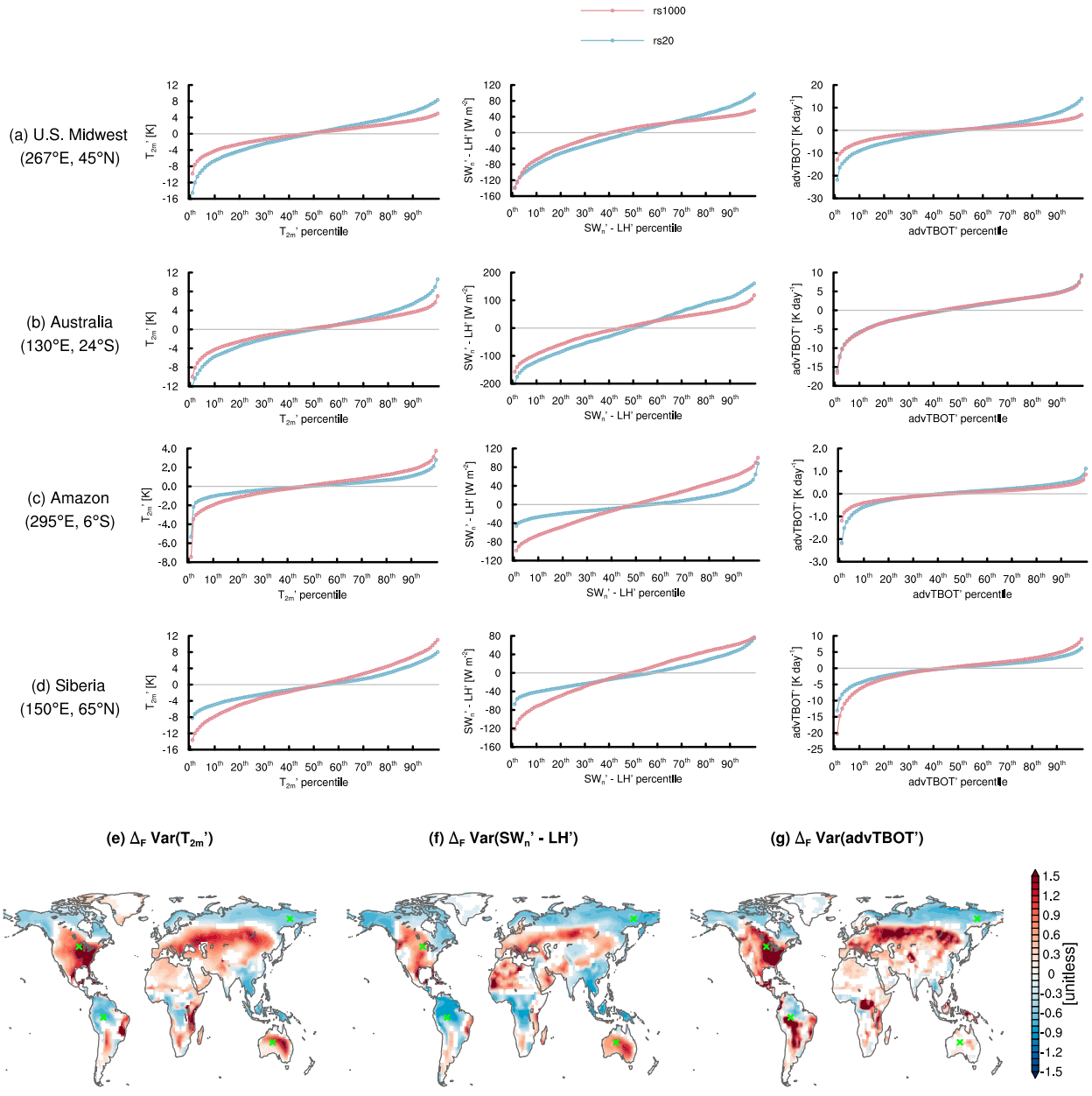

FIG. 13. Overview of responses of continental daily temperature variance to perturbations in the land surface evaporative resistance. The distribution of T'_{2m}, $SW'_n - LH'$, and advTBOT' at several case sites [denoted by green markers in (e)–(g)] are shown for (a) the U.S. Midwest (45°N, 267°E), (b) Australia (24°S, 130°E), (c) the Amazon (6°S, 295°E), and (d) Siberia (65°N, 150°E). The blue and red marker lines denote results from r_s20 to r_s1000, respectively. (e)–(g) Fractional changes [$\Delta_F = (r_s20 - r_s1000)/r_s1000$] of Var($T'_{2m}$), Var($SW'_n - LH'$), and Var(advTBOT'), respectively. Land areas where the variance change is not significant after accounting for a false discovery rate of 0.1 are masked in white.

and that we focus on the variance of daily temperature anomalies. Further, although $\Delta\mathrm{Var}(T'_{2m})$ can be understood from $\Delta\mathrm{Var}(SW'_n - LH')$ in response to the globally uniform r_s perturbations, we did not find a close correspondence between $\mathrm{Var}(SW'_n - LH')$ and $\mathrm{Var}(T'_{2m})$ in the mean state in our simulations. Still, it is interesting to note that though Vargas Zeppetello and Battisti (2020) focused on the temperature variance response to the greenhouse gas forcing while our work focuses on the effects of land surface forcing, their results agree with our finding if we view precipitation as a stand-in for LH.

6. Summary

This work explores the responses of summer daily continental temperature variance to perturbations in the land surface evaporative resistance (r_s), and discusses the underlying

mechanisms that drive the temperature variance change. We employ an idealized land surface model SLIM (Laguë et al. 2019) coupled to an atmospheric circulation model CAM6 within the CESM2 framework. We focused on two idealized scenarios, where r_s over the global land area is prescribed to 20 s m^{-1} (r_s20) and 1000 s m^{-1} (r_s1000), respectively. We first examined changes in the summer hydrology and surface climate when r_s decreases. Although soil moisture decreases everywhere in the low r_s case, changes in evaporation show an opposite sign between wetter areas and drier areas. Unlike wetter areas where decreasing r_s enhances evaporation, latent heat flux decreases in drier areas in the low r_s case, because soil moisture becomes critically low in drier areas and limits evaporation. Decreases in r_s lead to a global scale cooling in both surface and near-surface temperature, with the cooling magnitude being relatively small in drier areas such as the western United States, the Sahara Desert, central Asia, and southern Australia. We find that changes in the near-surface temperature can be largely understood from changes in surface energy fluxes. Decreasing r_s causes a global scale increase of low cloud cover and regional changes in both middle and high cloud cover, which collectively affect surface temperature due to both shortwave and longwave cloud radiative forcing. Changes in the surface turbulent heat fluxes, especially the evaporative cooling, also affect surface temperature. Overall, we find a close spatial correspondence between changes in the surface temperature and the combined effects of shortwave radiation and latent heat flux (i.e., $\mathrm{SW}_n - \mathrm{LH}$): regions where $\Delta(\mathrm{SW}_n - \mathrm{LH})$ is negative experienced significant cooling, while the cooling is largely dampened in regions where $\Delta(\mathrm{SW}_n - \mathrm{LH})$ is positive. Near-surface horizontal thermal advection appears to affect the summer mean state response as well. In particular, changes in thermal advection act to oppose the effects of $\Delta(\mathrm{SW}_n - \mathrm{LH})$ and leads to cooling in regions where $\Delta(\mathrm{SW}_n - \mathrm{LH})$ is positive. Discussion of a correlation metric $\rho(\mathrm{LH}', T'_{2\mathrm{m}})$ that captures soil moisture–atmosphere coupling strength suggests that temperature anomalies are strongly constrained by soil moisture availability in the low r_s case, while temperature variation in high r_s case may be affected more by atmospheric processes.

Decreasing r_s leads the summer temperature variance to increase in most extratropical land areas and decrease in the tropical and the northern high-latitude regions. We first sought to understand changes in the temperature variance through a surface energy balance framework. Given that changes in r_s can alter shortwave radiation (through changes in cloudiness) and evaporation (through changes in evaporation efficiency and soil moisture amount), we explored whether changes in temperature variance can be explained by changes in the combined variance of shortwave and latent heat fluxes. Our analysis suggests that changes in $\mathrm{Var}(\mathrm{SW}'_n - \mathrm{LH}')$ can indeed qualitatively explain changes in $\mathrm{Var}(T'_{2\mathrm{m}})$ over land, and the spatial cross correlation between the fractional changes in $\mathrm{Var}(\mathrm{SW}'_n - \mathrm{LH}')$ and $\mathrm{Var}(T'_{2\mathrm{m}})$ is 0.77. We further explored changes in the variance of horizontal thermal advection. Our results show a strong resemblance between changes in the variability of thermal advection and changes in temperature variance in the northern mid- to high latitudes. Correlations across land grid points along each latitude further indicate that changes in the advection variance amplified changes in the temperature variance in the Northern Hemisphere extratropical regions.

Several caveats of our work are worth mentioning. First, evaporation efficiency in the real world is affected by various factors, such as rooting depth, canopy water holding capacity, photosynthesis, and stomatal conductance. Unlike the more realistic land models in which different fluxes of canopy evaporation of intercepted water, transpiration, and soil evaporation are considered, SLIM aggregates these water fluxes into one bulk, canopy-level resistance. Second, land–atmosphere coupling has been shown to be model dependent (Koster et al. 2006; Seneviratne et al. 2010), and previous studies suggest models usually overestimate summer temperature variability compared to observations (Merrifield and Xie 2016; Mueller and Seneviratne 2014). Further, the ocean–atmosphere coupling, which is not considered in our current study, is suggested to be important in continental temperature variability (Davin and de Noblet-Ducoudré 2010). Finally, the precipitation response, which was a component of understanding the land surface hydrology changes (section 3a), could depend on the atmospheric model used in this study.

Our simulation with reduced evaporative resistance mimics a scenario with a worldwide cropping intensification. Mueller et al. (2016) suggest that cropping intensification in the Midwest can dampen summer heat extremes through enhanced evaporative cooling. One interesting result from their work is that the dampening effect of cropping intensification differs drastically between irrigated and rain-fed regions. Because soil moisture is always ample in irrigated regions, cropping intensification dampens hot extremes during both drought and nondrought years. Hot extremes in rain-fed regions, however, only experience evident dampening during nondrought years. In a similar vein, we find that the background soil moisture amount is critical in determining the response of temperature variance to perturbations in r_s. A competing effect between enhanced evaporation efficiency and reduced soil moisture amount emerges in regions with relatively limited soil moisture.

Finally, we note that the relative contributions of surface energy fluxes and thermal advection could differ between the low and high r_s cases. How the effects of different physical drivers on temperature variance and extremes evolve in a changing climate is still an open question. Wehrli et al. (2019) assessed contributions of different physical drivers to recent major heat waves in Europe and found that atmospheric circulation can be equally important as that of soil moisture to some heat wave anomalies. Our latitudinal correlation (Fig. 10b) and multiple linear regression analysis (Fig. 12b) also indicate that changes in the variance of thermal advection might have played an equally important role in driving changes in the temperature variance in northern extratropical land areas. Of particular interest for a future direction is to obtain a complete picture of the spatial distribution of the relative importance of land conditions and atmospheric circulations, and how they evolve in a changing climate.

Acknowledgments. W.K., K.A.M., and I.R.S. acknowledge support from the National Science Foundation (Award 1939988).

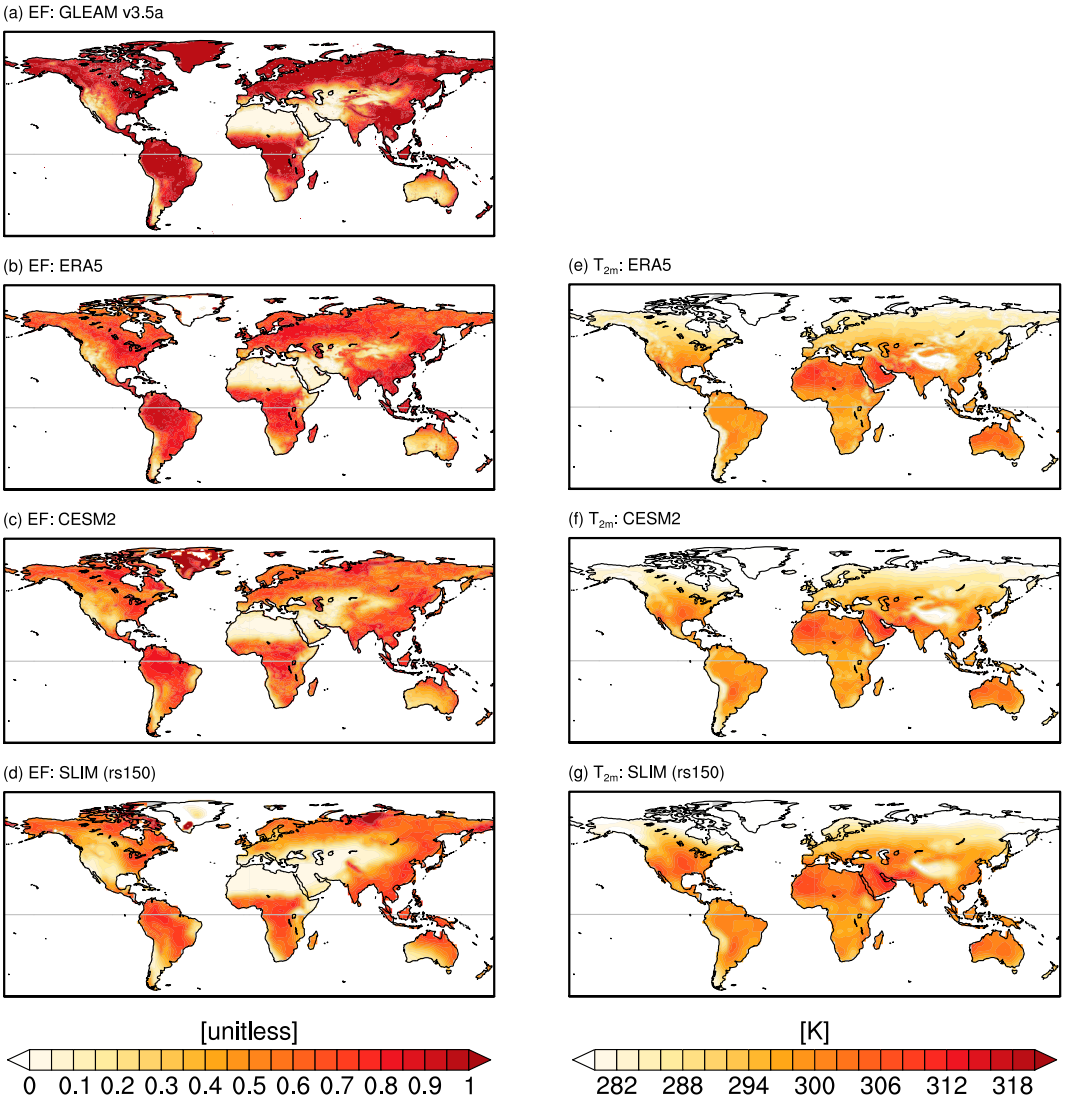

FIG. A1. Summertime climatology of (left) evaporative fraction (unitless) and (right) 2-m air temperature (K). (a) Evaporative fraction calculated from the GLEAM v3.5a dataset (1980–2020). Also shown are results from (b),(e) ERA5 (1979–2019), (c),(f) a CESM2-AMIP historical simulation (1950–2014), and (d),(g) SLIM run r_s150.

I.R.S. was supported by the National Center for Atmospheric Research (NCAR), which is a major facility sponsored by the National Science Foundation under the Cooperative Agreement 1852977. M.M.L. is supported by the James S. McDonnell Foundation. We thank Gordon Bonan for valuable discussions during the early stage of our experimental design. We would like to acknowledge high-performance computing support from Cheyenne (doi:10.5065/D6RX99HX) provided by NCAR's Computational and Information Systems Laboratory, sponsored by the National Science Foundation. We thank two anonymous reviewers for their constructive comments and suggestions. W.K. thanks Suqin Duan for helpful conversations in understanding land–atmosphere interaction.

Data availability statement. Scripts for creating the land surface forcing files and for setting up the SLIM simulations are available at https://github.com/wenwenkong/kong_etal_2022_jcli_t2m. The source code of SLIM is available at https://github.com/marysa/SimpleLand/. Detailed information of the CESM2 AMIP simulations can be found at https://data.ucar.edu/en/dataset/f-e21-fhist_bgc-f09_f09_mg17-cmip6-amip-001-cmip6-cesm2-amip-hindcast-1950-2014-with-interactiv3. The CESM2 AMIP simulations can be accessed from the Earth System Grid website at https://www.earthsystemgrid.org/dataset/ucar.cgd.cesm2.output.html or from NCAR's Cheyenne campaign storage in this path: /glade/campaign/collections/cmip/CMIP6/timeseries-cmip6/. The ERA5 dataset can be accessed from the European Centre for Medium-Range Weather

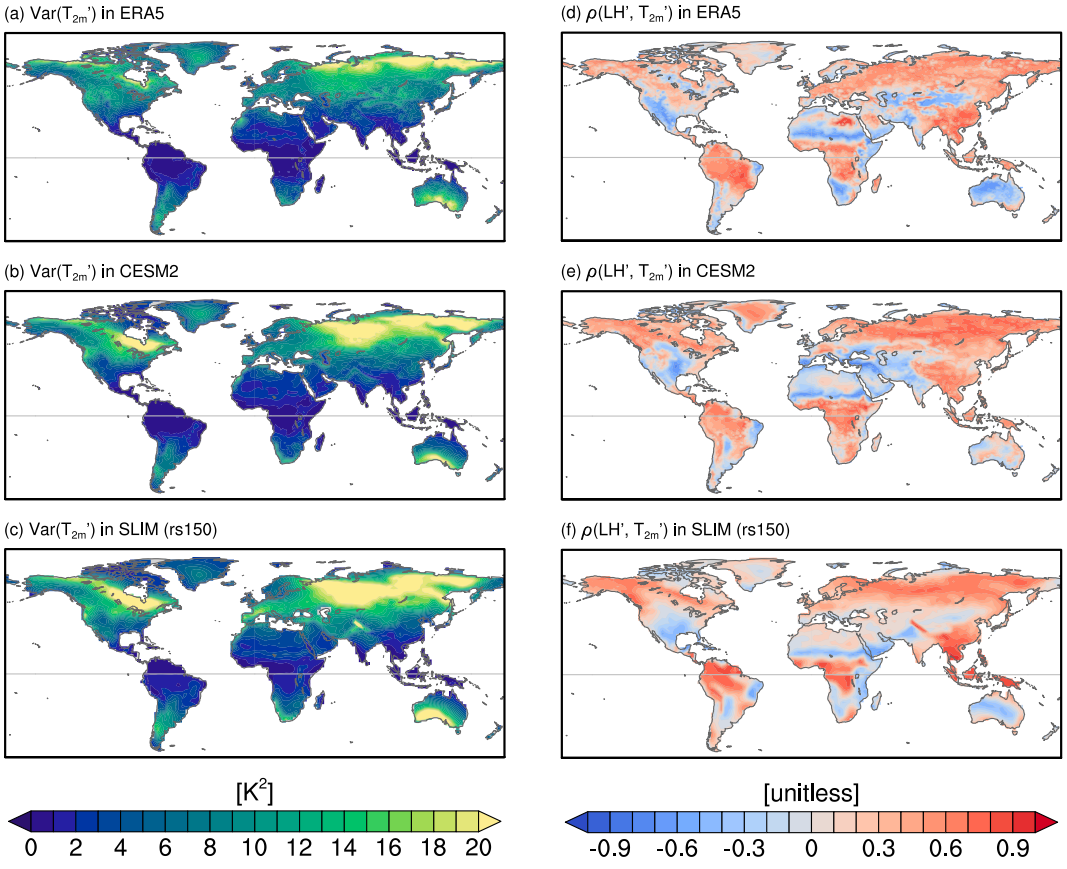

FIG. A2. Summertime variance of daily 2-m air temperature anomalies in (a) ERA-5, (b) CESM2, and (c) SLIM run r_s150, and the correlation between latent heat flux anomalies and temperature anomalies $\rho(\mathrm{LH}', T'_{2\mathrm{m}})$ in (d) ERA-5, (e) CESM2, and (f) SLIM run r_s150.

Forecasts (ECMWF), Copernicus Climate Change Service (C3S) at Climate Data Store (https://cds.climate.copernicus.eu/). The GLEAM v3.5a dataset can be downloaded from https://www.gleam.eu.

APPENDIX

Comparing SLIM to ERA5, GLEAM, and CESM2

Here we briefly discuss the representation of the climatology and variability of SLIM coupled with CAM6 at 1.9° × 2.5° in simulating the climatology and variability of summertime continental temperature. We use r_s150 to assess SLIM's performance as the prescribed r_s in this simulation is neither too low (compared to r_s20) nor too high (compared to r_s1000). Overall, our SLIM simulated EF and $T_{2\mathrm{m}}$ climatology agree well with the ERA5 dataset (Fig. A1). The spatial pattern of the SLIM and CAM6 simulated EF also largely agree with the GLEAM v3.5a dataset (Fig. A1a). However, both SLIM and CESM2 underestimate the EF and overestimate $T_{2\mathrm{m}}$, which is not surprising as climate models are known to suffer from warm biases in $T_{2\mathrm{m}}$ over midlatitude continents, especially in the U.S. Great Plains (Cheruy et al. 2014; Ma et al. 2014). Laguë et al. (2019) also noted the $T_{2\mathrm{m}}$ warm bias in SLIM. It is suggested that the EF underestimate is the dominant source of the warm temperature bias, and that the warm bias is more significant in Atmospheric Model Intercomparison Project (AMIP)-type simulations than those in the ocean–atmosphere coupled simulations (Ma et al. 2018). Compared to ERA5, both CESM2 and SLIM overestimate the temperature variability, especially in the northern mid- to high latitudes (Fig. A2), which has also been documented in previous studies (Merrifield and Xie 2016; Mueller and Seneviratne 2014). Sippel et al. (2017) suggest that some climate models overestimate summertime temperature variability because they fall too frequently into water-limited regimes. The land–atmosphere coupling strength indeed differs between ERA5 and model simulations (Figs. A2d–f). In particular, the temperature variance over the central United States being larger in CESM2 and SLIM likely results from the stronger land–atmosphere coupling in these models. Other factors that are not explored here (such as shortwave variability and atmospheric circulation) may also contribute to the temperature variance difference. Despite these biases compared to the ERA5 reanalysis dataset, the resemblance of the SLIM simulation compared to CESM2 suggests that although the land surface processes are highly simplified in SLIM, the model (prescribed with the land surface conditions used in our work) can still simulate reasonable surface climate and temperature variability.

REFERENCES

Andrade, C., S. M. Leite, and J. A. Santos, 2012: Temperature extremes in Europe: Overview of their driving atmospheric patterns. *Nat. Hazards Earth Syst. Sci.*, **12**, 1671–1691, https://doi.org/10.5194/nhess-12-1671-2012.

Baldwin, J. W., J. B. Dessy, G. A. Vecchi, and M. Oppenheimer, 2019: Temporally compound heat wave events and global warming: An emerging hazard. *Earth's Future*, **7**, 411–427, https://doi.org/10.1029/2018EF000989.

Berg, A., B. R. Lintner, K. L. Findell, S. Malyshev, P. C. Loikith, and P. Gentine, 2014: Impact of soil moisture–atmosphere interactions on surface temperature distribution. *J. Climate*, **27**, 7976–7993, https://doi.org/10.1175/JCLI-D-13-00591.1.

——, and Coauthors, 2015: Interannual coupling between summertime surface temperature and precipitation over land: Processes and implications for climate change. *J. Climate*, **28**, 1308–1328, https://doi.org/10.1175/JCLI-D-14-00324.1.

Bogenschutz, P. A., A. O. Gettelman, C. Hannay, V. E. Larson, R. B. Neale, C. Craig, and C.-C. Chen, 2018: The path to CAM6: Coupled simulations with CAM5.4 and CAM5.5. *Geosci. Model Dev.*, **11**, 235–255, https://doi.org/10.5194/gmd-11-235-2018.

Bonan, G. B., 1996: A land surface model (LSM version 1.0) for ecological, hydrological, and atmospheric studies: Technical description and user's guide. NCAR Tech. Note NCAR/TN-417+STR, 150 pp., https://doi.org/10.5065/D6DF6P5X.

——, 2016: *Ecological Climatology*. 3rd ed. Cambridge University Press, 692 pp., https://doi.org/10.1017/CBO9781107339200.

Branstator, G., and H. Teng, 2017: Tropospheric waveguide teleconnections and their seasonality. *J. Atmos. Sci.*, **74**, 1513–1532, https://doi.org/10.1175/JAS-D-16-0305.1.

Bretherton, C. S., 2014: Lecture 3: Statistical sampling uncertainty. University of Washington, 5 pp., https://atmos.washington.edu/~breth/classes/AM582/lect/lect3-notes.pdf.

Budyko, M. I., 1961: The heat balance of the Earth's surface. *Sov. Geogr.*, **2**, 3–13, https://doi.org/10.1080/00385417.1961.10770761.

Canadell, J. G., and M. R. Raupach, 2008: Managing forests for climate change mitigation. *Science*, **320**, 1456–1457, https://doi.org/10.1126/science.1155458.

Chan, D., A. Cobb, L. R. V. Zeppetello, D. S. Battisti, and P. Huybers, 2020: Summertime temperature variability increases with local warming in midlatitude regions. *Geophys. Res. Lett.*, **47**, e2020GL087624, https://doi.org/10.1029/2020GL087624.

Cheruy, F., J. L. Dufresne, F. Hourdin, and A. Ducharne, 2014: Role of clouds and land–atmosphere coupling in midlatitude continental summer warm biases and climate change amplification in CMIP5 simulations. *Geophys. Res. Lett.*, **41**, 6493–6500, https://doi.org/10.1002/2014GL061145.

——, ——, S. A. Mesbah, J. Y. Grandpeix, and F. Wang, 2017: Role of soil thermal inertia in surface temperature and soil moisture–temperature feedback. *J. Adv. Model. Earth Syst.*, **9**, 2906–2919, https://doi.org/10.1002/2017MS001036.

Collins, W. D., and Coauthors, 2004: Description of the NCAR Community Atmosphere Model (CAM 3.0). NCAR Tech. Note NCAR/TN-464+STR, 214 pp., https://doi.org/10.5065/D63N21CH.

Community Earth System Model developers and affiliates, 2019: f.e21.FHIST_bgc.f09_f09_mg17.CMIP6-AMIP.001 CMIP6 CESM2 AMIP hindcast (1950–2014) with interactive land (CLM5), data ocean, prescribed sea ice, and non-evolving land ice (CISM2.1). UCAR/NCAR-Climate and Global Dynamics Laboratory, accessed 7 November 2020, https://www.earthsystemgrid.org/dataset/ucar.cgd.cesm2.f.e21.FHIST_BGC.f09_f09_mg17.CMIP6-AMIP.001.html.

Compo, G. P., and P. D. Sardeshmukh, 2009: Oceanic influences on recent continental warming. *Climate Dyn.*, **32**, 333–342, https://doi.org/10.1007/s00382-008-0448-9.

Cowan, T., G. C. Hegerl, I. Colfescu, M. Bollasina, A. Purich, and G. Boschat, 2017: Factors contributing to record-breaking heat waves over the great plains during the 1930s dust bowl. *J. Climate*, **30**, 2437–2461, https://doi.org/10.1175/JCLI-D-16-0436.1.

Danabasoglu, G., and Coauthors, 2020: The Community Earth System Model version 2 (CESM2). *J. Adv. Model. Earth Syst.*, **12**, e2019MS001916, https://doi.org/10.1029/2019MS001916.

Davin, E. L., and N. de Noblet-Ducoudré, 2010: Climatic impact of global-scale deforestation: Radiative versus nonradiative processes. *J. Climate*, **23**, 97–112, https://doi.org/10.1175/2009JCLI3102.1.

Delworth, T., and S. Manabe, 1989: The influence of soil wetness on near-surface atmospheric variability. *J. Climate*, **2**, 1447–1462, https://doi.org/10.1175/1520-0442(1989)002<1447:TIOSWO>2.0.CO;2.

de Noblet-Ducoudré, N., and Coauthors, 2012: Determining robust impacts of land-use-induced land cover changes on surface climate over North America and Eurasia: Results from the first set of LUCID experiments. *J. Climate*, **25**, 3261–3281, https://doi.org/10.1175/JCLI-D-11-00338.1.

Devaraju, N., N. de Noblet-Ducoudré, B. Quesada, and G. Bala, 2018: Quantifying the relative importance of direct and indirect biophysical effects of deforestation on surface temperature and teleconnections. *J. Climate*, **31**, 3811–3829, https://doi.org/10.1175/JCLI-D-17-0563.1.

Dirmeyer, P. A., 2003: The role of the land surface background state in climate predictability. *J. Hydrometeor.*, **4**, 599–610, https://doi.org/10.1175/1525-7541(2003)004<0599:TROTLS>2.0.CO;2.

Findell, K. L., E. Shevliakova, P. C. D. Milly, and R. J. Stouffer, 2007: Modeled impact of anthropogenic land cover change on climate. *J. Climate*, **20**, 3621–3634, https://doi.org/10.1175/JCLI4185.1.

Fischer, E. M., and R. Knutti, 2015: Anthropogenic contribution to global occurrence of heavy-precipitation and high-temperature extremes. *Nat. Climate Change*, **5**, 560–564, https://doi.org/10.1038/nclimate2617.

——, and C. Schär, 2009: Future changes in daily summer temperature variability: Driving processes and role for temperature extremes. *Climate Dyn.*, **33**, 917, https://doi.org/10.1007/s00382-008-0473-8.

——, S. I. Seneviratne, D. Lüthi, and C. Schär, 2007a: Contribution of land–atmosphere coupling to recent European summer heat waves. *Geophys. Res. Lett.*, **34**, L06707, https://doi.org/10.1029/2006GL029068.

——, ——, P. L. Vidale, D. Lüthi, and C. Schär, 2007b: Soil moisture–atmosphere interactions during the 2003 European summer heat wave. *J. Climate*, **20**, 5081–5099, https://doi.org/10.1175/JCLI4288.1.

Garfinkel, C. I., and N. Harnik, 2017: The non-Gaussianity and spatial asymmetry of temperature extremes relative to the storm track: The role of horizontal advection. *J. Climate*, **30**, 445–464, https://doi.org/10.1175/JCLI-D-15-0806.1.

Gregory, J. M., and J. F. B. Mitchell, 1995: Simulation of daily variability of surface temperature and precipitation over Europe in the current and 2 × CO_2 climates using the UKMO climate

model. *Quart. J. Roy. Meteor. Soc.*, **121**, 1451–1476, https://doi.org/10.1002/qj.49712152611.

Guo, Z., and Coauthors, 2006: GLACE: The Global Land–Atmosphere Coupling Experiment. Part II: Analysis. *J. Hydrometeor.*, **7**, 611–625, https://doi.org/10.1175/JHM511.1.

Hersbach, H., and Coauthors, 2020: The ERA5 global reanalysis. *Quart. J. Roy. Meteor. Soc.*, **146**, 1999–2049, https://doi.org/10.1002/qj.3803.

Hirschi, M., and Coauthors, 2011: Observational evidence for soil-moisture impact on hot extremes in southeastern Europe. *Nat. Geosci.*, **4**, 17–21, https://doi.org/10.1038/ngeo1032.

Holmes, C. R., T. Woollings, E. Hawkins, and H. de Vries, 2016: Robust future changes in temperature variability under greenhouse gas forcing and the relationship with thermal advection. *J. Climate*, **29**, 2221–2236, https://doi.org/10.1175/JCLI-D-14-00735.1.

Hulley, G. C., B. Dousset, and B. H. Kahn, 2020: Rising trends in heatwave metrics across southern California. *Earth's Future*, **8**, e2020EF001480, https://doi.org/10.1029/2020EF001480.

Hutcheon, J. A., A. Chiolero, and J. A. Hanley, 2010: Random measurement error and regression dilution bias. *BMJ*, **340**, c2289, https://doi.org/10.1136/bmj.c2289.

Jaeger, E. B., and S. I. Seneviratne, 2011: Impact of soil moisture–atmosphere coupling on European climate extremes and trends in a regional climate model. *Climate Dyn.*, **36**, 1919–1939, https://doi.org/10.1007/s00382-010-0780-8.

Jeevanjee, N., P. Hassanzadeh, S. Hill, and A. Sheshadri, 2017: A perspective on climate model hierarchies. *J. Adv. Model. Earth Syst.*, **9**, 1760–1771, https://doi.org/10.1002/2017MS001038.

Katz, R. W., and B. G. Brown, 1992: Extreme events in a changing climate: Variability is more important than averages. *Climatic Change*, **21**, 289–302, https://doi.org/10.1007/BF00139728.

Kim, J. E., M. M. Laguë, S. Pennypacker, E. Dawson, and A. L. S. Swann, 2020: Evaporative resistance is of equal importance as surface albedo in high-latitude surface temperatures due to cloud feedbacks. *Geophys. Res. Lett.*, **47**, e2019GL085663, https://doi.org/10.1029/2019GL085663.

Klein, S. A., 1997: Synoptic variability of low-cloud properties and meteorological parameters in the subtropical trade wind boundary layer. *J. Climate*, **10**, 2018–2039, https://doi.org/10.1175/1520-0442(1997)010<2018:SVOLCP>2.0.CO;2.

Kooperman, G. J., M. S. Pritchard, T. A. O'Brien, and B. W. Timmermans, 2018: Rainfall from resolved rather than parameterized processes better represents the present-day and climate change response of moderate rates in the Community Atmosphere Model. *J. Adv. Model. Earth Syst.*, **10**, 971–988, https://doi.org/10.1002/2017MS001188.

Koster, R. D., and Coauthors, 2006: GLACE: The Global Land–Atmosphere Coupling Experiment. Part I: Overview. *J. Hydrometeor.*, **7**, 590–610, https://doi.org/10.1175/JHM510.1.

Kotz, M., L. Wenz, and A. Levermann, 2021: Footprint of greenhouse forcing in daily temperature variability. *Proc. Natl. Acad. Sci. USA*, **118**, e2103294118, https://doi.org/10.1073/pnas.2103294118.

Laguë, M. M., and A. L. S. Swann, 2016: Progressive midlatitude afforestation: Impacts on clouds, global energy transport, and precipitation. *J. Climate*, **29**, 5561–5573, https://doi.org/10.1175/JCLI-D-15-0748.1.

——, G. B. Bonan, and A. L. S. Swann, 2019: Separating the impact of individual land surface properties on the terrestrial surface energy budget in both the coupled and uncoupled land–atmosphere system. *J. Climate*, **32**, 5725–5744, https://doi.org/10.1175/JCLI-D-18-0812.1.

——, A. L. S. Swann, and W. R. Boos, 2021: Radiative feedbacks on land surface change and associated tropical precipitation shifts. *J. Climate*, **34**, 6651–6672, https://doi.org/10.1175/JCLI-D-20-0883.1.

Lawrence, D. M., and Coauthors, 2019: The Community Land Model version 5: Description of new features, benchmarking, and impact of forcing uncertainty. *J. Adv. Model. Earth Syst.*, **11**, 4245–4287, https://doi.org/10.1029/2018MS001583.

Lee, X., and Coauthors, 2011: Observed increase in local cooling effect of deforestation at higher latitudes. *Nature*, **479**, 384–387, https://doi.org/10.1038/nature10588.

Lenderink, G., A. van Ulden, B. van den Hurk, and E. van Meijgaard, 2007: Summertime inter-annual temperature variability in an ensemble of regional model simulations: Analysis of the surface energy budget. *Climatic Change*, **81**, 233–247, https://doi.org/10.1007/s10584-006-9229-9.

Linz, M., G. Chen, and Z. Hu, 2018: Large-scale atmospheric control on non-Gaussian tails of midlatitude temperature distributions. *Geophys. Res. Lett.*, **45**, 9141–9149, https://doi.org/10.1029/2018GL079324.

——, ——, B. Zhang, and P. Zhang, 2020: A framework for understanding how dynamics shape temperature distributions. *Geophys. Res. Lett.*, **47**, e2019GL085684, https://doi.org/10.1029/2019GL085684.

Lohmann, U., and J. Feichter, 2005: Global indirect aerosol effects: A review. *Atmos. Chem. Phys.*, **5**, 715–737, https://doi.org/10.5194/acp-5-715-2005.

Lorenz, R., E. L. Davin, and S. I. Seneviratne, 2012: Modeling land–climate coupling in Europe: Impact of land surface representation on climate variability and extremes. *J. Geophys. Res.*, **117**, D20109, https://doi.org/10.1029/2012JD017755.

Luyssaert, S., and Coauthors, 2014: Land management and land-cover change have impacts of similar magnitude on surface temperature. *Nat. Climate Change*, **4**, 389–393, https://doi.org/10.1038/nclimate2196.

Ma, H.-Y., and Coauthors, 2014: On the correspondence between mean forecast errors and climate errors in CMIP5 models. *J. Climate*, **27**, 1781–1798, https://doi.org/10.1175/JCLI-D-13-00474.1.

——, and Coauthors, 2018: CAUSES: On the role of surface energy budget errors to the warm surface air temperature error over the central United States. *J. Geophys. Res. Atmos.*, **123**, 2888–2909, https://doi.org/10.1002/2017JD027194.

Manabe, S., 1969: Climate and the ocean circulation. I. The atmospheric circulation and the hydrology of the Earth's surface. *Mon. Wea. Rev.*, **97**, 739–774, https://doi.org/10.1175/1520-0493(1969)097<0739:CATOC>2.3.CO;2.

Martens, B., and Coauthors, 2017: GLEAM v3: Satellite-based land evaporation and root-zone soil moisture. *Geosci. Model Dev.*, **10**, 1903–1925, https://doi.org/10.5194/gmd-10-1903-2017.

——, D. L. Schumacher, H. Wouters, J. Muñoz-Sabater, N. E. C. Verhoest, and D. G. Miralles, 2020: Evaluating the land-surface energy partitioning in ERA5. *Geosci. Model Dev.*, **13**, 4159–4181, https://doi.org/10.5194/gmd-13-4159-2020.

Meehl, G. A., and C. Tebaldi, 2004: More intense, more frequent, and longer lasting heat waves in the 21st century. *Science*, **305**, 994–997, https://doi.org/10.1126/science.1098704.

Merrifield, A. L., and S.-P. Xie, 2016: Summer U.S. surface air temperature variability: Controlling factors and AMIP simulation biases. *J. Climate*, **29**, 5123–5139, https://doi.org/10.1175/JCLI-D-15-0705.1.

Milly, P. C. D., and A. B. Shmakin, 2002: Global modeling of land water and energy balances. Part I: The Land Dynamics

(LaD) model. *J. Hydrometeor.*, **3**, 283–299, https://doi.org/10.1175/1525-7541(2002)003<0283:GMOLWA>2.0.CO;2.

Miralles, D. G., T. R. H. Holmes, R. M. De Jeu, J. H. Gash, A. G. C. A. Meesters, and A. J. Dolman, 2011: Global land-surface evaporation estimated from satellite-based observations. *Hydrol. Earth Syst. Sci.*, **15**, 453–469, https://doi.org/10.5194/hess-15-453-2011.

Mu, Q., M. Zhao, and S. W. Running, 2011: Improvements to a MODIS global terrestrial evapotranspiration algorithm. *Remote Sens. Environ.*, **115**, 1781–1800, https://doi.org/10.1016/j.rse.2011.02.019.

Mueller, B., and S. I. Seneviratne, 2014: Systematic land climate and evapotranspiration biases in CMIP5 simulations. *Geophys. Res. Lett.*, **41**, 128–134, https://doi.org/10.1002/2013GL058055.

Mueller, N. D., E. E. Butler, K. A. McKinnon, A. Rhines, M. Tingley, N. M. Holbrook, and P. Huybers, 2016: Cooling of US Midwest summer temperature extremes from cropland intensification. *Nat. Climate Change*, **6**, 317–322, https://doi.org/10.1038/nclimate2825.

Norris, J. R., 1998: Low cloud type over the ocean from surface observations. Part I: Relationship to surface meteorology and the vertical distribution of temperature and moisture. *J. Climate*, **11**, 369–382, https://doi.org/10.1175/1520-0442(1998)011<0369:LCTOTO>2.0.CO;2.

Panwar, A., A. Kleidon, and M. Renner, 2019: Do surface and air temperatures contain similar imprints of evaporative conditions? *Geophys. Res. Lett.*, **46**, 3802–3809, https://doi.org/10.1029/2019GL082248.

Pfahl, S., and H. Wernli, 2012: Quantifying the relevance of atmospheric blocking for co-located temperature extremes in the Northern Hemisphere on (sub-) daily time scales. *Geophys. Res. Lett.*, **39**, L12807, https://doi.org/10.1029/2012GL052261.

Pitman, A. J., 2003: The evolution of, and revolution in, land surface schemes designed for climate models. *Int. J. Climatol.*, **23**, 479–510, https://doi.org/10.1002/joc.893.

——, and Coauthors, 2009: Uncertainties in climate responses to past land cover change: First results from the LUCID intercomparison study. *Geophys. Res. Lett.*, **36**, https://doi.org/10.1029/2009GL039076.

Purdy, A. J., J. B. Fisher, M. L. Goulden, and J. S. Famiglietti, 2016: Ground heat flux: An analytical review of 6 models evaluated at 88 sites and globally. *J. Geophys. Res. Biogeosci.*, **121**, 3045–3059, https://doi.org/10.1002/2016JG003591.

Quesada, B., R. Vautard, P. Yiou, M. Hirschi, and S. I. Seneviratne, 2012: Asymmetric European summer heat predictability from wet and dry southern winters and springs. *Nat. Climate Change*, **2**, 736–741, https://doi.org/10.1038/nclimate1536.

Rasmijn, L. M., G. van der Schrier, R. Bintanja, J. Barkmeijer, A. Sterl, and W. Hazeleger, 2018: Future equivalent of 2010 Russian heatwave intensified by weakening soil moisture constraints. *Nat. Climate Change*, **8**, 381–385, https://doi.org/10.1038/s41558-018-0114-0.

Ruffault, J., and Coauthors, 2020: Increased likelihood of heat-induced large wildfires in the Mediterranean Basin. *Sci. Rep.*, **10**, 13790, https://doi.org/10.1038/s41598-020-70069-z.

Schär, C., P. L. Vidale, D. Lüthi, C. Frei, C. Häberli, M. A. Liniger, and C. Appenzeller, 2004: The role of increasing temperature variability in European summer heatwaves. *Nature*, **427**, 332–336, https://doi.org/10.1038/nature02300.

Schneider, T., T. Bischoff, and H. Płotka, 2015: Physics of changes in synoptic midlatitude temperature variability. *J. Climate*, **28**, 2312–2331, https://doi.org/10.1175/JCLI-D-14-00632.1.

Schwingshackl, C., M. Hirschi, and S. I. Seneviratne, 2018: Global contributions of incoming radiation and land surface conditions to maximum near-surface air temperature variability and trend. *Geophys. Res. Lett.*, **45**, 5034–5044, https://doi.org/10.1029/2018GL077794.

Screen, J. A., 2014: Arctic amplification decreases temperature variance in northern mid- to high-latitudes. *Nat. Climate Change*, **4**, 577–582, https://doi.org/10.1038/nclimate2268.

Seneviratne, S. I., D. Lüthi, M. Litschi, and C. Schär, 2006: Land–atmosphere coupling and climate change in Europe. *Nature*, **443**, 205–209, https://doi.org/10.1038/nature05095.

——, T. Corti, E. L. Davin, M. Hirschi, E. B. Jaeger, I. Lehner, B. Orlowsky, and A. J. Teuling, 2010: Investigating soil moisture–climate interactions in a changing climate: A review. *Earth-Sci. Rev.*, **99**, 125–161, https://doi.org/10.1016/j.earscirev.2010.02.004.

——, and Coauthors, 2012: Changes in climate extremes and their impacts on the natural physical environment. *Managing the Risks of Extreme Events and Disasters to Advance Climate Change Adaptation*, C. B. Field et al., Eds., Cambridge University Press, 109–230, https://doi.org/10.7916/d8-6nbt-s431.

——, and Coauthors, 2013: Impact of soil moisture–climate feedbacks on CMIP5 projections: First results from the GLACE-CMIP5 experiment. *Geophys. Res. Lett.*, **40**, 5212–5217, https://doi.org/10.1002/grl.50956.

Singh, N., A. Mhawish, S. Ghosh, T. Banerjee, and R. K. Mall, 2019: Attributing mortality from temperature extremes: A time series analysis in Varanasi, India. *Sci. Total Environ.*, **665**, 453–464, https://doi.org/10.1016/j.scitotenv.2019.02.074.

Sippel, S., J. Zscheischler, M. D. Mahecha, R. Orth, M. Reichstein, M. Vogel, and S. I. Seneviratne, 2017: Refining multi-model projections of temperature extremes by evaluation against land–atmosphere coupling diagnostics. *Earth Syst. Dyn.*, **8**, 387–403, https://doi.org/10.5194/esd-8-387-2017.

Stephens, G. L., and P. J. Webster, 1981: Clouds and climate: Sensitivity of simple systems. *J. Atmos. Sci.*, **38**, 235–247, https://doi.org/10.1175/1520-0469(1981)038<0235:CACSOS>2.0.CO;2.

Swann, A. L. S., I. Y. Fung, and J. C. H. Chiang, 2012: Mid-latitude afforestation shifts general circulation and tropical precipitation. *Proc. Natl. Acad. Sci. USA*, **109**, 712–716, https://doi.org/10.1073/pnas.1116706108.

Tamarin-Brodsky, T., K. Hodges, B. J. Hoskins, and T. G. Shepherd, 2020: Changes in Northern Hemisphere temperature variability shaped by regional warming patterns. *Nat. Geosci.*, **13**, 414–421, https://doi.org/10.1038/s41561-020-0576-3.

Teuling, A. J., and Coauthors, 2010: Contrasting response of European forest and grassland energy exchange to heatwaves. *Nat. Geosci.*, **3**, 722–727, https://doi.org/10.1038/ngeo950.

Vargas Zeppetello, L. R., and D. S. Battisti, 2020: Projected increases in monthly midlatitude summertime temperature variance over land are driven by local thermodynamics. *Geophys. Res. Lett.*, **47**, e2020GL090197, https://doi.org/10.1029/2020GL090197.

——, ——, and M. B. Baker, 2019a: The origin of soil moisture evaporation "regimes". *J. Climate*, **32**, 6939–6960, https://doi.org/10.1175/JCLI-D-19-0209.1.

——, A. Donohoe, and D. S. Battisti, 2019b: Does surface temperature respond to or determine downwelling longwave radiation? *Geophys. Res. Lett.*, **46**, 2781–2789, https://doi.org/10.1029/2019GL082220.

——, D. S. Battisti, and M. B. Baker, 2020: A new look at the variance of summertime temperatures over land. *J. Climate*, **33**, 5465–5477, https://doi.org/10.1175/JCLI-D-19-0887.1.

Vogel, E., M. G. Donat, L. V. Alexander, M. Meinshausen, D. K. Ray, D. Karoly, N. Meinshausen, and K. Frieler, 2019: The effects of climate extremes on global agricultural yields. *Environ. Res. Lett.*, **14**, 054010, https://doi.org/10.1088/1748-9326/ab154b.

von Storch, H., and F. W. Zwiers, 1999: *Statistical Analysis in Climate Research*. Cambridge University Press, 484 pp., https://doi.org/10.1017/CBO9780511612336.

Wallace, J. M., Y. Zhang, and J. A. Renwick, 1995: Dynamic contribution to hemispheric mean temperature trends. *Science*, **270**, 780–783, https://doi.org/10.1126/science.270.5237.780.

Wehrli, K., B. P. Guillod, M. Hauser, M. Leclair, and S. I. Seneviratne, 2019: Identifying key driving processes of major recent heat waves. *J. Geophys. Res. Atmos.*, **124**, 11 746–11 765, https://doi.org/10.1029/2019JD030635.

Wilks, D. S., 2016: "The stippling shows statistically significant grid points": How research results are routinely overstated and overinterpreted, and what to do about it. *Bull. Amer. Meteor. Soc.*, **97**, 2263–2273, https://doi.org/10.1175/BAMS-D-15-00267.1.

Zscheischler, J., R. Orth, and S. I. Seneviratne, 2015: A submonthly database for detecting changes in vegetation–atmosphere coupling. *Geophys. Res. Lett.*, **42**, 9816–9824, https://doi.org/10.1002/2015GL066563.